MOMSO 1.0 - a near-global, coupled biogeochemical ocean-circulation model configuration with realistic eddy kinetic energy in the Southern Ocean.

Heiner Dietze[1,2], Ulrike Löptien[1,2], and Julia Getzlaff[1]

[1]GEOMAR, Helmholtz Centre for Ocean Research Kiel, Düsternbrooker Weg 20, D-24105 Kiel, Germany.
[2]Institute of Geosciences, University of Kiel, Kiel, Germany.

Correspondence: H. Dietze
(hdietze@geomar.de)

Abstract

We present a new near-global coupled biogeochemical ocean-circulation model configuration. The configuration features a horizontal discretization with a grid spacing of less than $11\,km$ in the Southern Ocean and gradually coarsens in meridional direction to more than 200 km at 64° N where the model is bounded by a solid wall. The underlying code framework is GFDL's

5 Modular Ocean Model coupled to the **B**iology **L**ight **I**ron **N**utrients and **G**asses (BLING) ecosystem model of Galbraith et al. (2010). The configuration is cutting-edge in that it features both a relatively equilibrated oceanic carbon inventory and a realistic representation of eddy kinetic energy - a combination that has, to-date, been precluded by prohibitive computational cost. Results from a simulation with climatological forcing and a sensitivity experiment with increasing winds suggest that the configuration is suited to explore Southern Ocean Carbon uptake dynamics on decadal timescales. Further, the fidelity of

10 simulated bottom water temperatures off and on the Antarctic Shelf suggest that the configuration may be used to provide boundary conditions to ice-sheet models. The configuration is dubbed **MOMSO** a **M**odular **O**cean **M**odel **S**outhern **O**cean configuration.

1 Introduction

The Southern Ocean, also known as the Antarctic Ocean, comprises the southernmost waters of the World Oceans. It's southern

15 boundary is set by the Antarctic continent. As concerns its northern boundary to the Atlantic, Pacific and Indian Ocean, there is no consensus. One common definition is the location of the Subtropical Front (STF), which separates the relatively saline subtropical waters from the fresher sub-Antarctic waters. This definition is straightforward because it characterizes the transition from one oceanographic regime to another, distinctly different, one. However, because the position of the front varies with time, the definition adds complexity to certain analysis such as oceanic inventories. A pragmatic solution is to define a

20 fixed latitude as the northern boundary. We choose 40°S.

The atmospheric conditions in the Southern Ocean are characterized by frequent cyclonic storms that travel eastward around the Antarctic continent and high-pressure areas over the poles. This averages to a strong westerly wind belt between 40°S

and 60°S and rather weak and irregular polar easterlies from 60°S on southwards. The predominant low-frequency mode of atmospheric variability is summarized by the Southern Annular Mode (Limpasuvan and Hartmann, 1999; Marshall, 2003) which essentially describes the strength and position of the westerly wind belt.

The strong westerly wind belt drive the Antarctic Circumpolar Current (ACC), the "mightiest current in the oceans" (Pickard

5   and Emery, 1990) which is unobstructed by continents. The ACC circumnavigates the globe zonally and, thus, links the Atlantic, Pacific, and Indian Oceans. A northward Ekman transport (also driven by the westerlies) drives up- and downwelling (Marshall and Speer, 2012) and is part of a meridional overturning circulation, also known as Deacon Cell. The role of eddy induced transports that oppose the strength of the Deacon Cell is still under discussion (e.g., Hallberg and Gnanadesikan, 2006; Thompson et al., 2014; Tamsitt et al., 2017). Further complexity is added by sea-ice which modulates air-sea buoyancy fluxes

10 and thus effects and affects convection, a prerequisite for Antarctic Bottom Water (AABW) formation.

Being one of the few places world-wide where deep water (such as AABW) is formed, the Southern Ocean plays a major role in the global carbon budged. Convection events tap into the abyssal ocean and modulate the difference between atmospheric and oceanic CO_2 concentrations which drive net-air sea fluxes. A comprehensive quantitative understanding is still work in progress but the consensus is that the variability in the extent, to which deep-water masses in the Southern Ocean are isolated

15 from the atmosphere, is among the major drivers regulating atmospheric CO_2-variability (e.g., Anderson et al., 2009; van Heuven et al., 2014; Ritter et al., 2017). Consequently, the Southern Ocean has shifted into the limelight of climate research (DeVries et al., 2017; Tamsitt et al., 2017; Langlais et al., 2017, and many more).

As for now we know that the Southern Ocean accounts for almost half of the global oceanic CO_2 uptake from the atmosphere (Takahashi et al., 2012). But, there is concern that anticipated climate change (e.g., via changes of atmospheric circulation and

20 sea-ice cover) may trigger substantial changes in the Southern Ocean carbon budget (e.g., Heinze et al., 2015; Abernathey et al., 2016) such that the current rate of uptake may well decline in decades to come. Indications for the existence of such triggers have been revealed by observation-based atmospheric reanalysis products which show an ongoing strengthening and a poleward shift of the southern westerly winds since the 1970s (Thompson and Solomon, 2002).

This observed trend is projected by climate scenarios to intensify (e.g., Simpkins and Karpechko, 2012) and it is straight-

25 forward to assume that the associated wind-driven circulation impinges on biogeochemical dynamics and, eventually, on the oceanic carbon budget. A comprehensive understanding of the link between changing winds and oceanic upwelling of carbon-rich deep waters (which, in turn, affects surface saturation and net air-sea CO_2 exchange) is, however, work in progress. To this end, the role of mesoscale ocean eddies is especially uncertain: the current generation of coarse resolution (non-mesoscale-resolving) models suggests that a poleward shift and an intensification of the Southern Ocean westerlies results

30 in a strengthening of the subpolar meridional overturning cell (e.g., Saenko et al., 2005; Hall and Visbeck, 2002; Getzlaff et al., 2016) and, consequently, in increased upwelling of deep water south of the circumpolar flow, which is rich in dissolved inorganic carbon (e.g., Zickfeld et al., 2007; Lenton and Matear, 2007; Lovenduski et al., 2008; Verdy et al., 2007). The net effect being here that changes of the atmospheric circulation reduce the capability of the Southern Ocean to sequester carbon away from the atmosphere. Early on, however, there were indications (e.g., Böning et al., 2008; Hallberg and Gnanadesikan,

35 2006; Hogg et al., 2008; Screen et al., 2009; Thompson and Solomon, 2002) that this model-behavior is a spurious consequence

of the underlying eddy parameterization in coarse resolution models which can not afford to resolve mesoscale dynamics explicitly. To date we know that very different state-of-the-art approaches to parameterize eddies yield surprisingly similar sensitivities of oceanic carbon-inventories to changing winds Dietze et al. (2017). The question, however, as to how these results compare to high resolution coupled biogeochemical ocean circulation which actually resolve eddies explicitly, has not

5   been answered yet. The main reason being the prohibitive computational cost that is associated to equilibrating simulated dissolved inorganic carbon concentrations at depth.

In this study we present the model configuration MOMSO 1.0. The configuration features realistic levels and distributions of eddy kinetic energy. This suggests that the configuration explicitly resolves a substantial part of mesoscale-related variability rather than relying on parameterizing their effect. MOMSO is designed to explore the sensitivity Southern Ocean carbon uptake

10   to atmospheric changes on decadal scales. The configuration is rendered feasible by recent advances in compute hardware and, by chance, from its similarity with a spun-up coarse resolution model which delivered the initial conditions for the biogeochemical module. More specifically, we will showcase that the "level-of-equilibration" of simulated deep dissolved inorganic carbon allows to test the sensitivity of the Southern Ocean carbon budget to anticipated climate change patterns and include a preliminary result of a comparison to the results of a similar, but coarse resolution, model.

15   In addition, we showcase that MOMSO is potentially suited to explore the effects of changing eddying circulation patterns on basal melting because it features a realistic representation of Antarctic Continental Shelf Bottom Water (ASBW) temperatures at the seabed off Antarctica. The realistic seabed temperatures, in combination with its biogeochemical module, empowers MOMSO to explore feedback loops such as: atmospherically-driven changes in ocean-circulation drive additional heat supply which fuel basal melting. The buoyant lens of meltwater may, for one, suppress the AABW-formation (Williams et al., 2016).

20   This, in turn, effects oceanic carbon sequestration. Second, the meltwater carries bioavailable iron to the Southern Ocean - which affects oceanic primary productivity and the associated export of organic carbon to depth (Grotti et al., 2005; Lannuzel et al., 2008, 2010; Raiswell et al., 2008; Smith et al., 2007; Smith and Nelson., 1986; van der Merwe et al., 2009).

In summary, this study aims to (1) describe and present a new eddying coupled ocean-circulation biogeochemical model configuration, and (2) to depict potential applications and associated research questions. The project is dubbed **MOMSO**, a

25   configuration of GFDL's **M**odular **O**cean **M**odel version 4p1 with enhanced resolution in the **S**outhern **O**cean. The naming is an homage to the underlying framework, the MOM4p1 release of NOAAs Geophysical Fluid Dynamics Laboratory (GFDL) Modular Ocean Model (Griffies, 2009). The framework was chosen because of its exceptional documentation, maturity, modularity and user community. The ocean circulation model is coupled to a sea-ice model and the biogeochemical module. The latter has been developed by Galbraith et al. (2010).

30   The configuration MOMSO is distributed, free of charge, in a joint effort of the biogeochemical modelling group at the Helmholtz Centre for Ocean Research, Kiel, Germany and the Institute of Geosciences of Kiel University.

2   Model Setup

This study is based on simulations with the Modular Ocean Model (MOM), version MOM4p1 (Griffies, 2009). The configuration is near-global, bounded by Antarctica and $64°$N. In the Southern Ocean the horizontal resolution is higher than $11\,km$ up till $40°$S. The meridional grid resolution coarsens towards the North (Fig. 1). There are no open boundaries and there is no tidal forcing.

The biogeochmical model BLING, short for **B**iology **Li**ght **I**ron **N**utrients and **G**asses (Galbraith et al., 2010) is coupled online to the ocean-sea ice model. Atmospheric CO_2 concentrations are prescribed to a preindustrial level of $278\,ppmv$. The respective carbon inventories and fluxes are referred to as *natural carbon*.

The remainder of this section provides more details.

2.1   Grid and Bathymetry

The underlying bathymetry is ETOPO5 (c.f. Data Announcement 88-MGG-02, Digital relief of the Surface of the Earth. NOAA, National Geophysical Data Center, Boulder, Colorado, 1988). Using a bilinear scheme the bathymetry is interpolated onto an Arakawa B-grid (Arakawa and Lamp, 1977) with 2400×482 tracer grid boxes in the horizontal. The ocean-circulation and the sea-ice model share the same horizontal grid.

The vertical discretisation comprises a total of 55 levels. Fig. 1 shows the nominal depth and thickness of each level. The model bathymetry is smoothed with a filter similar to the Shapiro filter (Shapiro, 1970). The filter weights are 0.25, 0.5 and 0.25. The filtering procedure can only decrease the bottom depth, i.e. essentially, it fills rough holes. The filter is applied three times consecutively. The resulting bathymetry contained lakes which we filled after visual inspection. In addition, we filled narrow inlets which had a width of less than three grid boxes. In total, MOMSO has 42.429.759 wet tracer grid boxes.

We use the *zstar* coordinate (Stacey et al., 1995; Adcroft and Campin, 2004) in the vertical, i.e., the depth and thickness of each level varies with time. *zstar* ($z^\star$) is calculated as a function of nominal depth (z), water depth (H) and the free sea surface height (η) which varies with time:

$$z^\star = H\left(\frac{z - \eta}{H + \eta}\right) \tag{1}$$

(equation 6.6 in Griffies, 2009). The approach overcomes the problem with vanishing surface grid boxes which appears in generic z-level discretisation when sea surface height variations are of similar magnitude than the thickness of the uppermost grid box.

2.2   The Ocean Component

MOM4p1 is a z-coordinate, free surface ocean general circulation model which discretizes the ocean's hydrostatic primitive equations on a fixed Eulerian grid. The vertical mixing of momentum and scalars is parameterized with the K-Profile-Parameterization approach of Large et al. (1994) with the same parameters applied in eddy-permitting global configurations of Dietze and Kriest (2012); Dietze and Löeptien (2013); Dietze et al. (2014), and Liu et al. (2010). The relevant parameters are

(1) a critical bulk Richardson number of 0.3 and (2) a constant vertical background diffusivity and viscosity of $10^{-5}\ m^2/s$. The background values apply also below the surface mixed layer throughout the water column. Both parameterizations of the nonlocal and the double diffusive (vertical) scalar tracer fluxes are applied.

We apply a state-dependent horizontal Smagorinsky viscosity scheme (Griffies and Hallberg, 2000) to keep friction at the minimal level demanded by numerical stability. We use the PPM advection scheme (Colella and Woodward, 1984) for active tracers and a flux-limited scheme following Sweby (1984) for biogeochemical tracers. We do not apply an explicit horizontal background diffusivity other than the contribution that is implicit to the advection scheme.

Several decades into the spin-up the configuration became unstable in coarsely-resolved places where strong currents met rough topography. Setting an additional horizontal isotropic Laplacian Viscosity of $600\,m^2/s$ from 10°S to 50°N, of $1200\,m^2/s$ above 50°N and $1800\,m^2/s$ and above 60°N until the northern boundary of the model domain kept the respective oscillations in check. In addition we added Laplacian Viscosity at the exit of Drake Passage (Fig. 2).

2.3 The Sea Ice Component

The ocean component is coupled to a dynamical sea ice module, the GFDL Sea Ice Simulator (SIS). SIS uses elatic-viscous-plastic rheology adapted from Hunke and Dukowicz (1997). In the standard version, the simulated sea ice impacts sea surface height. This led to a viscous cycle at some places where sea ice attracts ever more sea ice resulting in unrealistic anomalies in sea surface height. We solved this problem by switching to levitating sea ice (by applying a small change to the code).

2.4 The Biogeochemical Component

In our setup, the ocean component is coupled to the BLING ecosystem model of Galbraith et al. (2010). BLING is a prognostic model that, in the basic version, explicitly resolves four biogeochemical tracers: dissolved inorganic phosphorous, dissolved organic phosphorous, dissolved iron and dissolved oxygen. In this study we use BLING in conjunction with a carbon module that explicitly resolves dissolved inorganic carbon and alkalinity as described, e.g., in Bernadello et al. (2014).

The design idea behind the "reduced-tracer" model BLING is a low computational cost and yet, complex-enough, framework to be utilized in high-resolution configurations. Our choice of BLING is motivated by it's fidelity which is comparable to much more complex (and computationally expensive) models (Galbreith et al., 2015). Further, the choice allows for a comparison with the coarse-resolution setup described in Dietze et al. (2017) which uses the exact same BLING configuration.

2.5 Initial Conditions and Spin-up Procedure

The circulation model starts from rest (i.e. initial velocities are nil) with initial values for temperature and salinity taken from WOA2009 (Locarnini et al., 2010; Antonov et al., 2009, respectively). After 20 years of physics-only spin-up, the biogeochemical model is hooked on. The initial conditions for the biogeochemical tracers are interpolated from the fully spun-up coarse resolution configuration used by Dietze et al. (2017) (their "FMCD" simulation) which is, apart from the spacial discretization (and related parameters), identical to the MOMSO configuration. This procedure accelerates the equilibration of the carbon

dynamics substantially compared to using observational products. After a subsequent 60 year-long spin-up with on-line bio-geochemistry the model allows already (as we will put forward in Section 3.2) for an investigation of circulation-driven decadal changes of the Southern Ocean Carbon Budget.

2.6 Boundary Conditions and Sponges

5   The boundaries towards the Arctic (i.e. the northern end of the model domain shown in Fig. 1) are closed (i.e. they are represented by solid and flat walls). Temperature and salinity are restored to climatological estimates (Locarnini et al., 2010; Antonov et al., 2009) in so-called sponge zones located in the coarse-resolution domain. The sponge zones along with restoring timescales are shown in Fig. 3. The purpose of these sponges is to ensure realistic deep-water characteristics even though northern-hemisphere deep-water formation processes are handicapped by the combination of coarse resolution with the absence
10   of eddy-parameterizations.

  At the air-sea boundary we apply climatological atmospheric conditions taken from the Corrected Normal Year Forcing (COREv2 Large and Yeager, 2004). In addition we apply a surface salinity restoring to climatological values (Antonov et al., 2009) with a timescale of 1/2 year throughout the model domain.

  Atmospheric CO_2 concentrations are prescribed to a preindustrial level of $278\,ppmv$. Thus the simulated oceanic carbon is
15   also referred to as *natural carbon*. Biogeochemical air-sea fluxes (of iron) are identical to the ones applied in Galbraith et al. (2010) and Dietze et al. (2017).

  This paper describes output from two simulations dubbed REF and WIND. Both simulations share the same 80 year spin-up described in Sect. 2.5. WIND branches off from REF during the nominal year 1980 and is exposed to ever increasing wind speeds south of 40°S. The increase is linear at a rate of 14% in 50 years, consistent with results from a reanalysis of the period
20   1958 to 2007 (Lovenduski et al., 2013).

  IO-related hardware problems caused data loss. REF covers the period from 1980 to 2024, WIND covers 1980 to 2022 only.

3   Results

In the following we evaluate our model (simulation REF) by comparing our climatological results from the nominal years 1980 - 2024 to observational data (Sec. 3.1). One problem is the tradeoff between data density and the length of the period the data is
25   representative for. For any given year data densities are typically insufficient to compile a comprehensive 3-dimensional gridded data product. Binning data of several years into one product closes spacial data gaps, but then, this blurs the referencing to an ever (anthropogenically-driven) changing system state. This problem is especially pronounced in the Southern Ocean where in-situ data acquisition is complicated by hostile environmental conditions.

  The climatological atmospheric boundary conditions which drive our ocean model are representative for the period 1958-
30   2000. Climatological data products are typically biased in that they contain more recent data being the result of recent techno-logical advances (such as the development of autonomous platforms). Hence, a model evaluation is not straightforward and it is difficult to define meaningful model-data misfit metrics. Our pragmatic approach to this problem is to put plots of observed

and modeled properties which are typically found in respective publications side to side. Further, we make an effort to put our climatological model results into the context of observed trends/interannual variability.

In addition to the observations being moving targets, unfortunately, the climatological simulation REF does also exhibit a certain amount of drift. This drift is associated to a spin-up procedure that is of finite duration (i.e. starting from rest, it has

5 only been integrated for a finite number of model years). Subsection 3.2 puts this drift into perspective by comparing the drift in simulation REF with the temporal evolution of the simulation WIND which is driven by idealized (but realistic) wind anomalies over the Southern Ocean.

Hence, by putting the configuration's sensitivity in relation to its persistent drift Subsection 3.2 provides a measure of the signal-to-noise ratio.

10 We close this Section in 3.3 with technical issues.

3.1 Evaluation of the Climatological Simulation

The major aim of our model setup is to explore the role of mesoscale features, or, eddies in determining the CO_2-uptake of the Southern Ocean. One hypothesis this model is set-up to test is whether spatially-unresolved dynamics in IPCC-type coarse resolution models biases their carbon uptake sensitivity. In order to come to a meaningful conclusion on this, our

15 high-resolution model has to perform with a fidelity similar or superior to that of IPCC-type coarse resolution models. In the following we list and explain our choice of model assessments which we deem relevant in this respect. Please note, that a comprehensive coarse versus high resolution comparison is beyond the scope of this high-resolution model description.

– **Ocean circulation** (Sec. 3.1.1) which, e.g., effects the transport of carbon-rich deepwater to the surface, shapes the locations of fronts and constitutes a major pathway for nutrients that are essential for phytoplankton growth. For the

20   evaluation of surface currents, we use exemplary snapshots showcasing main circulation paths and spacial variability along with climatological sea surface height which is indicative for the barotropic circulation. More quantitative measures of transport characteristics are provided for the ACC (Drake Passage transport) and the Southern Ocean meridional overturning circulation. Further, we assess the strength of the cyclonic Ross and Weddell polar gyres which are formed by interactions between the ACC and the Antarctic continental shelf. Special emphasis is here on the larger Weddell

25   Gyre. This gyre entrains heat and salt from the ACC and carries them to the Antarctic continental shelves, where deep and bottom waters are produced and, thus, establish an intermittent connection between the atmosphere (surface ocean) and the deep oceanic carbon (nutrient) pool.

– **Eddy kinetic energy** (EKE, Sec. 3.1.2), which is an important measure for the mesoscale activity and thus a key proxy for realistically reproducing eddy-dynamics. At the surface the EKE can be derived from the variability of the sea surface

30   height (SSH), a measure that can be directly observed from space by satellite altimetry.

– **Temperatures** (Sec. 3.1.3), which determines the rate of biological turn-over (like most chemical reactions), affects the solubility pump of carbon and is related to the density of sea water. Cooling typically results in a reduction of buoyancy

and causes convection. Spatial temperature gradients are associated to geostrophic circulation (if they are not salinity-compensated). Further, sea surface temperature (SST) serves as a proxy for the realism of the surface mixed layer depth whose dynamics is a major process involved in the supply of nutrients from depth to the sun-lit surface ocean. The sea surface temperature (SST) can be directly observed from space and, therefore, is available in an unrivaled (compared to in-situ measured properties) spacial and temporal resolution. Temperatures at depth are important for basal melting and, thus, are related to the formation rate of Antarctic Bottom Water (AABW). AABW formation, in turn, affects the solubility and biotic pump of carbon.

– **Salinity** (Sec. 3.1.4) is related to the density of sea water. Saltening by brine rejection can cause convection, meltwater on the other hand can build lenses thus increasing the local stability of the water column which prevents vertical mixing. Spatial salinity gradients are associated to geostrophic circulation (if they are not temperature-compensated).

– **Sea Ice** (Sec. 3.1.5) caps the direct exchange between atmosphere and ocean and thus controls the air-sea gas exchange of CO_2. It also modulates the air-sea buoyancy forcing by, e.g., insulating the surface from heat loss or by brine rejection during ice formation. Further, it shields the surface water from solar irradiance and hampers the assimilation of CO_2 by autotrophic plankton.

– **Nutrients** (Sec. 3.1.6) which are essential to the growth of autotrophic plankton and whose availability exert major control on the biological pump. The most important macronutrient is bioavailable phosphorous such as phosphate (PO_4) because its availability is essential to all phytoplankton (and cyanobacteria). The distribution of PO_4 is determined by the interplay of ocean circulation transporting PO_4 dissolved in sea water and marine biota which utilize phosphorous to build biomass (typically at the surface) and release PO_4 in the course of degradation of organic material (typically at depth). In addition we assess simulated iron concentrations since, the Southern Ocean is well-known for being a site where this is limiting the growth of autotrophs (Boyd and Ellwood, 2010).

3.1.1 Ocean Circulation

Fig. 4 shows simulated climatological sea surface height (SSH) along with an estimate based on observations from space. The remarkable similarity between the two showcases that the major (barotropic) circulation patterns are well represented by the model - even in the coarse-resolution domain far north from the Southern Ocean.

Fig.5 shows exemplary snapshots of the surface velocities as observed from space (left, AVISO) and simulated (right, MOMSO). The boundary conditions of the model are not identical to the atmospheric boundary conditions on that specific day and the highly non-linear characteristics of eddy-dynamics renders an "eddy-to-eddy" similarity without data assimilation impossible. So the purpose of Fig.5 is to demonstrate the similarity of patterns and the major transport pathways which coincide remarkably. The closeup into the Agulhas retroflection zone (Fig. 6) highlights that this remarkable similarity is sustained right up into the transition to coarser, non-eddy-resolving resolution.

Fig. 7 shows a more quantitative circulation measure for the Drake Passage transport. (Here we refer to the reference simulation only; simulation WIND is discussed in Section 3.2.) The simulated Drake Passage transport averages at 99 Sv

(nominal years 1980–2023). This is biased low compared to observational estimates that range from 110 to $170\,Sv$ (Withworth (1983) for 1979; Cunningham et al. (2003) for 1993–2000; Chidichima et al. (2014) for 2007–2011). Similar biases have been reported in other high-resolution configurations and may, according to Dufour et al. (2015), be related to a deficient representation of the overflow of dense waters, formed along the Antarctic coasts. If so, the ACC bias may well be endemic to
5   z-level models which struggle to represent complex topography (in comparison to more elaborate numerical approaches such as, e.g., finite elements). A comprehensive investigation is beyond the scope of this manuscript. But, still, the problem is an intriguing one – especially since, historically, (coarse resolution) models started out from an opposing bias dubbed Hidaka's Dilemma (Hidaka and Tsuchiya, 1953), where an excessive ACC transport could, only by application of unrealistically high friction, be fenced into realistic bounds.

10   In terms of meridional overturning in the Southern Ocean our model values are consistent with the Southern Ocean State Estimate of Mazloff et al. (2010): Mazloff et al. (2010) find a surface meridional overturning cell across 32°S of $12\pm12\,Sv$ and an abyssal cell of $13\pm6\,Sv$. We find a climatological mean value for the upper cell of $12\pm4\,Sv$ and $8\pm3\,Sv$ for the lower cell.

In terms of transports of the Weddell and Ross gyre our simulation is slightly biased high. In the Weddell gyre we simulate
15   $70\,Sv$ while published estimates range from $40\pm8\,Sv$ (Southern Ocean State Estimate, Mazloff et al., 2010) to $56\pm10Sv$ (recent SODA estimate Yongliang et al., 2016) 55.9 $\pm9.8Sv$ and $61-66\,Sv$ (Schröder and Fahrbach, 1999). In the Ross gyre we simulate $35\,Sv$ while published estimates range from $20\pm5\,Sv$ (Mazloff et al., 2010) to $15-30\,Sv$ (Chu and Fan, 2007) and $37\pm6\,Sv$ (Yongliang et al., 2016).

3.1.2 Eddy kinetic energy and sea surface height

20   Fig. 8 shows that the simulated climatological EKE reproduces the observed amplitudes and spatial patterns. Overall we conclude that the energetics of simulated mesoscale has realistic levels and we see no evidence of a general low bias. This suggests that our spacial resolution in the Southern Ocean is high enough to allow for a meaningful investigation of eddy-driven processes. A caveat here is that the observed EKE may be biased low as suggested by, e.g., Fratantoni (2001).

3.1.3 Temperature

25   Fig. 9 shows a comparison of the simulated SST with WOA09 (Locarnini et al., 2010) and ARGO float-based (Roemmich and Gilson, 2009) observations. The overall pattern is well reproduced - an exception being a local unusual high bias of about 3°C close to the Antarctic coast (between 120°E and 160°E) which we relate to an underestimation in sea ice coverage (c.f., Sect. 3.1.5).

On average, however, the simulated Southern Ocean SSTs (Fig. 10) are within the observational range (although at at the
30   lower edge) of the years 1960 to 2010 (Fig. 11 - calculated from HadISST, Rayner et al., 2003)), which is another indication of an overall good representation of the modelled SST.

Fig. 12 shows the simulated and observed (Schmidtko et al., 2014) temperatures of the Antarctic Continental Shelf Bottom Water (ASBW). The simulated temperatures are generally in good agreement with the observations.

3.1.4 Sea Surface Salinity

Fig. 13 shows a comparison of the simulated climatological mean sea surface salinity (SSS) with three observation-based products (WOA09 (Antonov et al., 2009), ARGO (Roemmich and Gilson, 2009) and SMOS (Köhler et al., 2015)). Within the spatially highly-resolved Southern Ocean the simulated sea surface salinity is in very good agreement with the observations. Towards the north, where the resolution coarsens the model fidelity disintegrates; particularly in the Atlantic, and Indic sector, the model is biased low.

On average the simulated Southern Ocean SSS is biased low (compare reference in Fig. 14) compared to recent observational estimates during 2005 – 2017 (Fig. 15). The underlying reason is subject to current investigation. For know, Fig. 14 suggests that increasing winds can increase simulated SSSs up to observed values. This could be interpreted as a mismatch between climatological forcing and observation period. In any case, Fig. 14 suggests that the surface salinity restoring (c.f. Section 2.6) is weak enough to allow for substantial SSS dynamics.

3.1.5 Sea Ice

Figure 16 shows a comparison of the simulated number of sea ice-covered months per year with an observation estimate (HadISST Rayner et al., 2003). Overall the agreement is good with the following exception: (1) The Weddell and Ross Sea the ice coverage is underestimated by two months. We speculate that this triggers elevated air-sea momentum fluxes and, eventually, biases the respective gyre strengths high (c.f. Section 3.1.1). (2) Overall the simulated ice extent is biased high (compare Fig. 17, black line to Fig. 18). This may (or may not) be associated with a mismatch between climatological forcing and observation period. In any case Fig. 17 suggests that increasing the wind speeds to levels being more representative for the time period of observations shown in Fig. 18 alleviates the model bias.

3.1.6 Nutrients

Simulated Southern Ocean PO_4 surface concentrations are biased low by down to 0.6 $mmol\,P/m^2$ locally (Fig. 19 a, c). The reason is not straightforward to identify because it could be associated to a deficient physical module, a deficient biogeochemical module, or both. In the following we will present an indication that the problem is associated to a deficient formulation of iron limitation, argue why the formulation of light-limitation is unlikely to be the main problem, voice a caveat, and, finally, put the model-data misfit into perspective.

The uptake of PO_4 at the sun-lit surface by autotrophic phytoplankton is known to be limited by the availability of light and the availability of the micronutrient iron (in the Southern Ocean). Fig. 20 features a comparison of simulated iron concentrations with observations. Even though the spacial and temporal coverage of iron measurements is still sparse (because iron is expensive to measure) the emerging pattern is one where the simulated biotic iron-drawdown at the surface appears to be too strong. Surface iron concentrations are biased low, just like the PO_4 concentrations and they appear so throughout an annual cycle. Such deficient model behavior can be caused by insufficient throttling of phytoplankton growth by both iron and light limitation. Looking closer in seasonal model-data misfits, however, suggests that a deficient iron limitation is more likely to

be the cause: The dependency of growth (and associated micro- and macronutrient drawdown at the surface) is known to be a highly nonlinear function of environmental drivers. We find that the bias in surface PO_4 concentrations is almost constant over the course of a seasonal cycle (Fig. 19 d), even though the photosynthetically available radiation varies dramatically from season to season in the respective latitudes (also because radiation experienced by phytoplankton cells dispersed in surface wa-

5   ters, is a function of the seasonally varying surface mixed layer depth). By chance, this could be the result of nonlinear forcing modulating a deficient nonlinear formulation of PO_4-limitation such that the model bias stays constant over a wide range of environmental conditions (here seasons). But this is unlikely. Looking into the seasonal bias of simulated iron concentrations (Fig. 20 d) we find that it varies substantially from season to season compared to the respective PO_4 variability (Fig. 19 d) – just as is expected when a deficient nonlinear model formulation is exposed to substantial variations in driving environmental

10   conditions.

A caveat remains. Simulated phosphate concentrations at depth (Fig. 19) are also biased low. This may be associated to a biological pump that is controlled by a deficient iron module. Equally likely, however, is that the biases at depth are caused by a deficient representation of ocean physics and associated abyssal circulation pathways.

In summary, the model's fidelity in reproducing observed patterns of biogeochemical properties is state-of-the-art (being non-

15   judgmental here). It is comparable to the coarse resolution twin (with twin referring to the biogeochemical model) configuration described in Dietze et al. (2017).

3.2 Sensitivity Experiment (WIND) versus (Reference) model drift

In the following we analyze the results of a sensitivity experiment. Simulation WIND differs from REF in that it branches off from REF while being driven by linearly increasing winds (c.f. Section 2.6). The prescribed rate of increase is comparable to

20   observed rates in the last decades. For this reasons we have referred to some of the WIND results in Section 3.1 already. The purpose there being to relate model-data mismatches to potentially mismatching (climatological) model forcing.

In the following the focus differs. We aim to showcase that the sensitivity of our model-configuration to a typical decadal change in boundary conditions is high relative to persistent model drift.

As the winds increase, the Southern Ocean overturning increases Fig. 21. The respective trend in the maximum overturning

25   is clearly distinguishable from the very weak drift of the reference simulation (Fig. 22). Locally, the wind-induced increase in overturning exceeds $0.3\,Sv\,yr^{-1}$ (Fig. 23). Averaged over the Southern Ocean, the overturning results in a surface cooling and saltening (Fig. 10). Both, the cooling and the saltening signals are clearly distinguishable from the very weak trend of the reference simulation.

Close to Antarctica the winds transport warmer waters to the surface where they melt (prevent) ice (formation). Fig. 17

30   shows that this trend is clearly distinguishable from the variability in the reference simulation.

Surprisingly, this does also apply to simulated trends in the temperature of the Antarctic Continental Shelf Bottom Water (ASBW) which, naturally, take much longer to equilibrate than surface processes. Fig. 24 compares the remaining model drift (panel a) to the drift-corrected trend in the sensitivity experiment WIND (panel b). The emerging pattern corresponds in amplitude well to observed values, while the sign is reversed. We thus speculate that observed changes of ASWB temperatures

can not only be attributed to the recent increases in wind-strength. In any case, Fig. 24 suggests that the equilibration of the model has set in sufficiently so that model responses to decadal forcing variability are detectable.

A caveat here is the ACC transport through Drake passage. Both simulations WIND and the reference feature a comparable and relatively strong drift (Fig.7).

5　The above mentioned trends in ocean (circulation) physics and changes in the sensitivity experiment WIND have their counterparts in the dynamics of biogeochemical processes. Some of these equilibrate quickly, such as surface nutrients or biomass while others are associated with long timescales. Carbon dynamics is notorious in that respect and this, for decades, has hindered the interpretation (and development) of eddy-resolving coupled ocean-circulation biogeochemical carbon models. To this end the results summarized in Fig. 25 are exceptional: the remaining drift in the MOMSO reference simulation is only

10　$1.0\,PgC/(1000\,yr^2)$ which allows for a clear detection of the effect of increasing winds in simulation WIND which yields a substantially larger decline of $5.0\,PgC/(1000\,yr^2)$.

MOMSO is very similar to the model configurations in Dietze et al. (2017). Further, Dietze et al. (2017) features the same simulations (i.e. a reference and WIND). This allows for a comparison of the high-resolution MOMSO simulations with coarse resolution, non-eddying simulations. Surprisingly, the two configurations yield very similar results: Dietze et al. (2017) find

15　a decreasing trend between 4.2 and $5.4\,PgC/(1000\,yr^2)$ depending on the underlying eddy-parameterization while MOMSO yields a drift-corrected $5\,PgC/(1000\,yr^2 - 1\,PgC/(1000\,yr^2) = 4\,PgC/(1000\,yr^2))$. A comprehensive comparison is a natural application of MOMSO but beyond the scope of this manuscript.

3.3　Computational cost

Initial development, testing and spin-up of the physical configuration was carried out on two 32-core workstations, based

20　on a 6320 AMD Opteron (Abu Dhabi) (8-core CPU, 2.80 GHz, 16MB L3 Cache, DDR3 1600) interconnected with a QDR InfiniBand. As of 2013 the system cost ≈ Euros 10.000,-. The fully coupled ocean-circulation biogeochemical model has been run at a supercomputing centre (project shk00027 at the *Norddeutscher Verbund für Hoch- und Höchstleistungsrechnen, HLRN*). Fig. 26 documents excellent parallel performance up to 500 tasks - a setting which optimized our throughput on the machine/queueing system. On 500 Intel Xeon CPU E5-2670 cores (Sandy Bridge) it takes 10 hours to simulate one year.

25　Referring to pricing published by HLRN in 2018 this amounts to ≈ Euros 250,- per integrated model year. We use compiler settings that optimize for computational efficiency. They violate computational reproducibility. A description of the associated computational uncertainty is provided in Section 3.8 of Dietze et al. (2014) which use the same code (applied to a different domain).

4　Summary and conclusions

30　We set out to develop a near-global coupled ocean-circulation biogeochemical model which explicitly resolves – in contrast to relying on respective parameterizations – effects of mesoscale eddy-dynamics on the uptake of carbon in the Southern Ocean. The setup is dubbed MOMSO with MOM referring to the underlying framework (GFDL's modular ocean model

version MOM4p1) and SO referring to the Southern Ocean. We use the biogeochemical/carbon module BLING developed by Galbraith et al. (2010).

Overall, we find in a climatological simulation (REF) an impressively eddying surface circulation that is in good agreement with observations from space. Further, simulated temperatures and sea surface salinity show a close agreement with observa-

5   tions. Sea-ice cover is biased high but is still in the range of observed values during particularly cold winters. A remaining caveat is a low bias in the Drake Passage ($99\,Sv$ compared to observational estimates ranging from 110 to $170\,Sv$).

The simulated biogeochemistry is also biased. Surface phosphate concentrations are too low in the Southern Ocean which is indicative of a deficient formulation of the limitation of phytoplankton growth. Seasonally varying biases in simulated surface iron concentrations suggest that the problem is associated to an, up-to-date, uncomprehensive quantitative understanding of

10   iron-dynamics. The model performance with respect to biogeochemistry is similar to what is state-of-the-art in coarse resolution models (e.g., Dietze et al., 2017).

MOMSO is a quantum leap in the field of eddying coupled ocean-circulation biogeochemical carbon modeling in that it allows to investigate the effects of decadal changes in atmospheric boundary conditions on the oceanic carbon uptake. Previous attempts have been hindered by the computational cost that is associated to run simulations into a semi-equilibrated state which

15   features trends considerably lower than the climate signals (as effected by prescribed anomalies in boundary conditions) under investigation. To this end MOMSO benefitted from: (1) an ever increasing ease of access to computing power that is associated to Moore's law and (2) the fortunate coincidence that the spun-up coarse resolution restart from Dietze et al. (2017) was close enough to the equilibrated high-resolution state of MOMSO.

In this study we showcased that the remaining drift in MOMSO's Southern Ocean carbon uptake is substantially lower than

20   changes driven by typical decadal variability of atmospheric variations. We illustrate that the respective sensitivity experiment is suitable for a comparison to coarser-resolution model versions and present a first impression in Fig. 25. Similarly we find that the drift in simulated temperatures of the Antarctic Continental Shelf Bottom Water is small enough to allow to link atmospheric decadal variability to oceanic temperature variations at the boundary to ice shelves around Antarctica.

We illustrate that the respective sensitivity experiment is suitable for a comparison to coarser resolution model versions and

25   present a first impression in Fig. 25.

On a final note, the computational cost associated with integrating MOMSO is substantial. With present-day hardware full spin-ups are in the 5-figure Euro range so that extensive tuning of the biogeochemical model, which still features some substantial misfits to observations, is uneconomical. Starting from the already spun-up state presented here, however, is in the reasonable range of 2500,- Euros per decade. The corresponding energy needs (operation only) are of the order of $1000\,kWh$

30   per decade. Using a carbon intensity of $450\,gCO_2/kWh$ (e.g., Moro and Lonza, 2018) this yields an emission of around 0.5 tons of CO_2 per simulated decade.

Code and data availability. The circulation model code MOM4p1 is distributed by NOAA's Geophysical Fluid Dynamics Laboratory (http://www.gfdl.noaa.gov/fms). We use the original code without applying any changes to it apart from very minor changes (≈ 10 lines of code)

which levitate sea ice (c.f., Sect. 2.3) and increase local viscosity (c.f., Sect. 2.2 and 2.5). The respective code, initial conditions, forcing, namelists, and model output is accessible via http://data.geomar.de/thredds/catalog/open_access/dietze_et_al_2018_gmd/catalog.html.

Author contributions. H. Dietze and U. Löptien have been involved in setting up and running the model configuration. All three authors contributed to the interpretation of model results, to outlining and writing of the paper.

5 *Competing interests.* The authors declare that they have no conflict of interest.

Geoscientific
Model Development
Discussions

References

Abernathey, R. P., Cerovecki, I., Holland, P. R., Newsom, E. Mazloff, M., and Talley, L. D.: Water-mass transformation by sea ice in the upper branch of the Southern Ocean overturning, Nature, 9, https://doi.org/10.1038/ngeo2749, 2016.

Adcroft, A. and Campin, J.-M.: Rescaled height coordinates for accurate representation of free-surface flows in ocean circulation models, Ocean Modeling, 7, 269–284, https://doi.org/10.1016/j.ocemod.2003.09.003, 2004.

Anderson, R. F., Ali, S., Bradtmiller, L. I., Nielsen, S. H. H., Fleisher, M. Q., Anderson, B. E., and Burckle, L. H.: Wind-driven upwelling in the Southern Ocean and the deglacial rise in atmospheric CO_2, Science, 323, 1443–1448, https://doi.org/10.1126/science.1167441, 2009.

Antonov, J. I., Seidov, D., Boyer, T. P., Locarnini, A., Mishonov, A. V., Garcia, H. E., Baranova, O. K., Zweng, M. M., and Johnson, D. R.: World Ocean Atlas 2009, Volume 2: Salinity. S. Levitus, Ed. NOAA Atlas NESDIS 69, U.S. Government Printing Office, Washington, D.C., 184 pp, 2010.

Arakawa, A. and Lamb, V. R.: Computational design of the basic dynamical processes of the UCLA general circulation model, Methods in Computational Physics, J. Chang, Ed., Vol. 17, Academic Press, 173–265, 1977.

Bernardello, R., Marinov, I., Palter, J. P., Sarmiento, J. L., Galbraith, E. D., and Slater, R. .D.: Response of the Ocean Natural Carbon Storage to Projected Twenty-First-Century Climate Change, J. Climate, 27, 2033–2053, https://doi.org/10.1175/JCLI-D-13-00343.1, 2014.

Böning, C. W., Dispert, A., Visbeck, M., Rintoul, S. R., and Schwarzkopf, F. U: The response of the Antarctic Circumpolar Current to recent climate change, Nature Geosci., 1, 864–869, https://doi.org/10.1038/ngeo362, 2008.

Boyd, P. W. and Ellwood, M. J.: The biogeochemical cycle of iron in the ocean, Nature Geosci., 3, 675–682, https://doi.org/10.1038/ngeo964, 2010.

Chu, P. C. and Fan, C.: An inverse model for calculation of global volume transport from wind and hydrographic data, Journal of Marine Systems, 65(1-4), 376–399, https://doi.org/10.1016/j.jmarsys.2005.06.010, 2007.

Chidichimo, M. P., Donohue, K. A., Watts, D. R., and Tracey, K. L.: Baroclinic transport time series of the Antarctic Circumpolar Current measured in Drake Passage, J. Phys. Oceanogr., 44, 1829–1853, https://doi.org/10.1175/JPO-D-13-071.1, 2014.

Colella, P., and Woodward, P. R.: The Piecewise Parabolic Method (PPM) for Gas-Dynamical Simulations. Journal of Computational Physics, 54, 174–201, 1984.

Cunningham, S. A., Alderson, S. G., King, B. A., and Brandon, M.A.: Transport and variability of the Antarctic Circumpolar Current in the Drake Passage, J. Geophys. Res., 108, https://doi.org/10.1029/2001JC001147, 2003.

DeVries, T., Holzer, M., and Primeau, F.: Recent increase in oceanic carbon uptake driven by weaker upper-ocean overturning, Nature, 542, https://doi.org/10.1038/nature21068, 2017.

Dietze, H., and Kriest, I.: [137]Cs off Fukushima Dai-ichi, Japan - model based estimates of dilution and fate. Ocean Science, 8, 319–332, https://doi.org/10.5194/os-8-319-2012, 2012.

Dietze, H., and Löeptien U.: Revisiting "nutrient trapping" in global coupled biogeochemical ocean circulation models. Global Biogeochemical Cycles, 27, 1–20, https://doi.org/10.1002/gbc.20029, 2013.

Dietze, H., Löptien, U., and Getzlaff, K.: MOMBA 1.1 - a high-resolution Baltic Sea configuration of GFDL's modular ocean model. Geoscientific Model Development, 7, 1713-1731, https://doi.org/10.5194/gmd-7-1713-2014, 2014.

Dietze, H., Getzlaff, J., and Lötien, U.: Simulating natural carbon sequestration in the Southern Ocean: on uncertainties associated with eddy parameterizations and iron deposition, Biogeosciences, 14, 1–16, https://doi.org/10.5194/bg-14-1-2017.

Dufour, C., et al.: Role of mesoscale eddies in cross-frontal transport of heat and biogeochemical tracers in the Southern Ocean, J. Phys. Oceanogr., 45, 3057–3081, https://doi.org/10.1175/JPO-D-14-0240.1, 2015.

Fratantoni, D. M.: North Atlantic surface circulation during the 1990's observed with satellite-tracked drifters, J. Geophys. Res., 106, 22067–22093, https://doi.org/10.1029/2000JC000730, 2001.

5   Galbraith, E. D., Gnanadesikan, A., Dunne, J. P., and Hiscock, M. R.: Regional impacts of iron-light colimitation in a global biogeochemical model, Biogeosciences, 7, 1043–1064, https://doi.org/10.5194/bg-7-1043-2010, 2010.

Galbraith, E. D., Dunne, J. P., Gnanadesikan, A., Slater, R. D., Sarmiento, J. L., Dufour, C. O., de Souza, G. F., Bianchi, D., Claret, M., Rodgers, K. B., and Marvasti, S. S.: Journal of Advances in Modeling Earth Systems, 7, 2012–2018, https://doi.org/10.1002/2015MS000463, 2015.

10   Garcia, H. E., Locarnini, R. A., Boyer, T. P., and Antonov, J. I.: World Ocean Atlas 2009, Volume 4: Nutrients (phosphate, nitrate, silicate), edited by: Levitus, S., NOAA Atlas NESDIS 71, U.S. Government Printing Office, Wahsington, D.C., 398 pp., 2010.

Getzlaff, J., Dietze, H., and Oschlies, A.: Simulated effects of southern hemispheric wind changes on the Pacific oxygen minimum zone, Geophys. Res. Lett., 43, 728–734, https://doi.org/10.1002/2015GL066841, 2016.

Griffies, S. M.: Elements of MOM4p1. GFDL Ocean Group Technical Report No. 6. NOAA/Geophysical Fluid Dynamics Laboratory, 444

15   pages, Version prepared on December 16, 2009.

Griffies, S. M. and Hallberg, R. W.: Biharmonic friction with a Smagorinsky-like viscosity for use in large-scale eddy-permitting ocean models, Mon. Weather Rev., 128, 2935–2946, 2000.

Grotti, M., F. Soggia, C. Ianni, and Frache, R.: Trace metals distribution in coastal sea ice of Terra Nova Bay, Ross Sea, Antarctica, Antarct. Sci., 17(2), 289–300, https://doi.org/10.1017/S0954102005002695, 2005.

20   Hall, A. and Visbeck, M.: Synchronous variability in the Southern Hemisphere atmosphere, sea ice, and ocean resulting from the Annular Mode, J. Climate, 15, 3043–3057, https://doi.org/10.1175/1520- 0442(2002)015<3043:SVITSH>2.0.CO, 2002.

Hallberg, R. and Gnanadesikan, A.: The role of eddies in determining the structure and response of the wind-driven southern hemisphere overturning: results from the modeling eddies in the southern ocean (MESO) project. J. Phys. Oceanogr. 36, 2232–2252, https://doi.org/10.1175/JPO2980.1, 2006.

25   Heinze, C., Meyer, S., Goris, N., Anderson, L., Steinfeldt, R., Chang, N., Le Quéré, C. and Bakker, D. C. E.: The ocean carbon sink – impacts, vulnerabilities and challenges, Earth System Dynamics, 6, https://doi.org/10.5194/esd-6-327-2015, 2015.

Hidake, K. and Tsuchiya, M.: On the Antarctic Circumpolar Current, Journal of Marine Research, 12, 214–222, 1953.

Hogg, A. McC., Meredith, M. P., Blundell, J. R., and Wilson, C.: Eddy heat flux in the Southern Ocean: Response to variable wind forcing, J. Climate, 21, 608–620, https://doi.org/10.1175/2007JCLI1925.1, 2008.

30   Hunke, E. C. and Dukowicz, J. K.: An Elastic-Viscous-Plastic Model for Sea Ice Dynamics. Journal of Physical Oceanography, 27, 1849–1867, 1997.

Köhler, J., Martins, M. S., Serra, N., and Stammer, D.: Quality assessment of spaceborne sea surface salinity observations over the northern North Atlantic. J. Geophys. Res. Oceans, 120, 94–112, https://doi.org/doi:10.1002/ 2014JC010067, 2015.

Langlais, C. E., Lenton, A., Matear, R., Monselesan, D. and Legresy, B., Cougnon, E., and Rintoul, S.: Stationary Rossby waves dominate

35   subduction of anthropogenic carbon in the Southern Ocean, Nature, 7, https://doi.org/10.1038/s41598-017-17292-3, 2017.

Lannuzel, D., V. Schoemann, J. de Jong, L. Chou, B. Delille, S. Becquevort, and Tison, J.: Iron study during a time series in the western Weddell pack ice, Mar. Chem., 108(1–2), 85–95, 2008.

Lannuzel, D., V. Schoemann, J. de Jong, B. Pasquer, P. van der Merwe, F. Masson, J.-L. Tison, and Bowie, A.: Distribution of dissolved iron in Antarctic sea ice: Spatial, seasonal, and interannual variability, J. Geophys. Res., 115, G03022, https://doi.org/10.1029/2009jg001031, 2010.

Large, W. G., McWilliams, J. C., and Doney, S. C.: Oceanic vertical mixing – A review and a model with nonlocal boundary-layer parameterization. Reviews of Geophysics, 32, 4, 363–403, 1994.

Large, W. G. and Yeager, S. G.: Diurnal to decadal global forcing for ocean and sea-ice models: the data sets and flux climatologies. NCAR Technical Note,TN-460, 2004.

Lenton, A. and Matear, R. J.: Role of the southern annular mode 80 (SAM) in Southern Ocean CO_2 uptake, Global Biogeochem. Cy., 21, https://doi.org/10.1029/2006GB002714, 2007.

Locarnini, R. A., Mishonov, A. V., Antonov, J. I., Boyer, T. P., Garcia, H. E., Baranova, O. K., Zweng, M. M., and Johnson, S. G: World Ocean Atlas 2009, Volume 1: Temperature. S. Levitus, Ed. NOAA Atlas NESDIS 69, U.S. Government Printing Office, Washington, D.C., 184 pp, 2010.

Lovenduski, N. S., Gruber, N., and Doney, S. C.: Toward a mechanistic understanding of the decadal trends in the Southern Ocean carbon sink, Global Biogeochem. Cy., 22, https://doi.org/10.1029/2007GB003139, 2008.

Lovenduski, N. S., Long, M. C., Gent, P. R., and Lindsay, K.: Multi-decadal trends in the advection and mixing of natural carbon in the Southern Ocean, Geophys. Res. L., 40, 139–142, https://doi.org/10.1029/2012GL054483, 2013.

Limpasuvan, V. and D. L. Hartmann, D. L.: Eddies and the annular modes of climate variability, Geophys. Res. Lett., 26, 3133–3136, https://doi.org/10.1029/1999GL010478, 1999.

Liu, N., Eden, C., Dietze, H., Wu, D., and Lin, X.: Model-based estimates of the heat budget in the East China Sea. Journal of Geophysical Research Oceans, 115, C08026, https://doi.org/10.1029/2009JC005869, 2010.

Marshall, G. J.: Trends in the Southern Annular Mode from observations and reanalyses, Journal of Climate, 16, 4134–4143, https://doi.org/10.1175/1520-0442(2003)016<4134:TITSAM>2.0.CO;2, 2003.

Marshall J. and Speer K.: Closure of the meridional overturning circulation through Southern Ocean upwelling, Nat. Geosci. 5, 171–180, https://doi.org/10.1038/ngeo1391, 2012.

Mazloff, M. R., Heimbach, P., and Wunsch, C.: An Eddy-Permitting Southern Ocean State Estimate. J. Phys. Oceanogr., 40, 880–899, https://doi.org/10.1175/2009JPO4236.1, 2010.

Mawji, E., et al.: The GEOTRACES Intermediate Data Product 2014, Marine Chemistry, 177, 1–8, https://doi.org/10.1016/j.marchem.2015.04.005, 2015.

Moro, A., and Lonza, L.: Electricity carbon intensity in European Member States: Impacts on GHG emissions of electric vehicles, Transp. Res. D Transp. Environ., 64, 5–14, https://doi.org/10.1016/j.trd.2017.07.012, 2018.

Pickard, G. L., and Emery, W. J.: Descriptive Physical Oceanography, An Introduction. Permagon Press, 5th Edition, 173-76, 1990.

Raiswell, R., Benning, L. G., Tranter, M., and Tulaczyk, S.: Bioavailable iron in the Southern Ocean: The significance of the iceberg conveyor belt, Geochem. Trans., 9(1), 7, https://doi.org/10.1186/1467-4866-9-7, 2008.

Rayner, N. A., Parker, D. E., Horton, E. B., Folland, C. K., Alexander, L. V., Rowell, D. P., Kent, E. C., and Kaplan, A.: Global analyses of sea surface temperature, sea ice, and night marine air temperature since the late nineteenth century, J. Geophys. Res., 108, D14, https://doi.org/10.1029/2002JD002670, 2003.

Ritter, R., Landschützer, P., Gruber, N.,Fay, A. R., Iida, Y., Jones, S., Nakaoka, S., Park, G.-H., Peylin, P., Rödenbeck, C., Rodgers, K. B., Shutler, J. D., and Zeng, J.: Observation-based trends of the Southern Ocean carbon sink. Geophysical Research Letters, 44, 12,339-12,348, https://doi.org/10.1002/2017GL074837, 2017.

Roemmich, D. and Gilson, J.: The 2004-2008 mean and annual cycle of temperature, salinity, and steric height in the global ocean from the
5   Argo Program. Progress in Oceanography, 82, 81–100, https://doi.org/10.1016/j.pocean.2009.03.004, 2009.

Saenko, O. A., Fyfe, J. C., and England, M. H.: On the response of the oceanic wind-driven circulation to atmospheric CO_2 increase, Clim. Dynam., 25, 415–426, https://doi.org/10.1007/s00382-005- 0032-5, 2005.

Screen, J. A., Gillett, N. G., Stevens, D. P., Marshall, G. J., and Roscoe, H. K.: The role of eddies in the Southern Ocean temperature response to the Southern Annular Mode, J. Climate, 22, 806–818, https://doi.org/10.1175/2008JCLI2416.1, 2009.

10   Schmidtko, S., Heywood, K. J., Thompson, A. F., and Aoki, S.: Multidecadal warming of Antarctic waters, Science, 346, 6214, 1227-1231, https://doi.org/10.1126/science.1256117, 2014.

Schröder M. and Fahrbach E.: On the structure and the transport of the eastern Weddell Gyre, Deep Sea Research Part II: Topical Studies in Oceanography, 46(1-2), 501–527, 1999.

Shapiro, R, 1970. Smoothing, filtering, and boundary effects, Reviews of Geophysics and Space Physics, 8, 2, 359–387.

15   Smith, K., Robison, B. H., Helly, J. J., Kaufmann, R. S., Ruhl, H. A., Shaw, T. J., Twining, B. S., and Vernet, M.: Free-drifting icebergs: Hot spots of chemical and biological enrichment in the Weddell Sea, Science, 317(5837), 478–482, https://doi.org/10.1126/science.1142834.

Smith, W. and Nelson, D.: Importance of ice edge phytoplankton production in the Southern Ocean, BioScience, 36(4), 251–257, 1986.

Simpkins, G. R. and Karpechko, A. Y.: Sensitivity of the southern annular mode to greenhouse gas emission scenarios, Clim. Dynam., 38, 563–572, https://doi.org/10.1007/s00382-011-1121-2, 2012.

20   Stacey, M. W., Pond, S., and Nowak, Z. P.: A numerical model of the circulation in Knight Inlet British Columbia, Canada, J. Phys. Oceanogr., 25, 1037–1062., 1995.

Sweby, P. K.: High Resolution Schemes Using Flux Limiters for Hyperbolic Conservation Laws. SIAM Journal on Numerical Analysis, 21, 5m 995–1011, 2012.

Tagliabue, A., Mtshali, T., Aumont, O., Bowie, A. R., Klunder, M. B., Roychoudhury, A. N., and Swart, S.: A global compilation of dissolved
25   iron measurements: focus on distributions and processes in the Southern Ocean, Biogoesciences, 9, 2333–2349, https://doi.org/10.5194/bg-9-2333-2012, 2012.

Tamsitt V., Drake, H. F., Morrison, A. K., Talley, L. D., Dufour, C. O., Gray, A. R., Griffies, S. M., Mazloff, M. R., Sarmiento, J. L., Wang, J., Weijer, W.: Spiraling pathways of global deep waters to the surface of the Souther Ocean. Nature Communications, 8, 172, https://doi.org/10.1038/s41467-017-00197-0, 2017.

30   Takahashi, T., C. Sweeney, B. Hales, D.W. Chipman, T. Newberger, J.G. Goddard, R.A. Iannuzzi, and Sutherland, S. C.: The changing carbon cycle in the Southern Ocean, Oceanography 25(3):26–37, https://doi.org/10.5670/oceanog.2012.71, 2012.

Thompson, D. W. J. and Solomon, S.: Interpretation of Recent Southern Hemisphere Climate Change, Science 296, 895, https://doi.org/10.1126/science.1069270, 2002.

Thompson, D. W. J., Solomon, S., Kushner, P. J., England, M. H., Grise, K. M., and Karoly, D. J.: Signatures of the Antarctic ozone hole in
35   Southern Hemisphere surface climates change, Nat. Geosci., 4, 741–749, https://doi.org/10.1038/NGEO1296,2014.

van Heuven, S. M., Hoppema, M., Jones, E. M., and de Baar, H. J.: Rapid invasion of anthropogenic CO_2 into the deep circulation of the Weddell Gyre, Philos. Trans. R. Soc. A, 372(2019), 20130,056, https://doi.org/10.1098/rsta.2013.0056, 2014.

van der Merwe, P., Lannuzel, D., Nichols, C. A. M., Meiners, K., Heil, P., Norman, L., Thomas, D. N., and Bowie, A. R.: Biogeochemical observations during the winter-spring transition in East Antarctic sea ice: Evidence of iron and exopolysaccharide controls, Mar. Chem., 115(3–4), 163–175, 2009.

Verdy, A., Dutkiewicz, S., Follows, M. J., Marshall, J., and Czaja, A.: Carbon dioxide and oxygen fluxes in the Southern Ocean: Mechanisms
5   of interannual variability, Global Biogeochem. Cy., 21, https://doi.org/10.1029/2006GB002916, 2007.

Williams, G. D., Herraiz-Borreguero, L., Roquet, F., Tamura, T., Ohshima, K. I., Fukamachi, Y., Fraser, A. D., Gao, L., Chen, H., McMahon, C. R., Harcourt, R., and Hindell, M.: The suppression of Antarctic bottom water formation by melting ice shelves in Prydz Bay, Nature Communications, 7, https://doi.org/10.1038/ncomms12577, 2016.

Whithworth, T.: Monitoring the transport of the Antarctic Circumpolar Current at Drake Passage, J. Phys. Oceanogr., 13, 2045–2057,
10   https://doi.org/10.1175/1520-0485(1983)013,2045: MTTOTA.2.0.CO;2, 1983.

Yongliang, D., Hongwei, L., Weidong, Y., and Yijun, H.: The mean properties and variations of the Southerm Hemisphere subpolar gyres estimated by Simple Ocean Data Assimilation (SODA) products. Acta Oceanol. Sin., 35, 7, 8–13, https://doi.org/10.1007/s13131-016-0901-2, 2016.

Zickfeld, K., Fyfe, J. C., Saenko, O. A., Eby, M., and Weaver, A. J.: Response of the global carbon cycle to human-induced changes in
15   Southern Hemisphere winds, Geophys. Res. Lett., 34, https://doi.org/10.1029/2006GL028797, 2007.
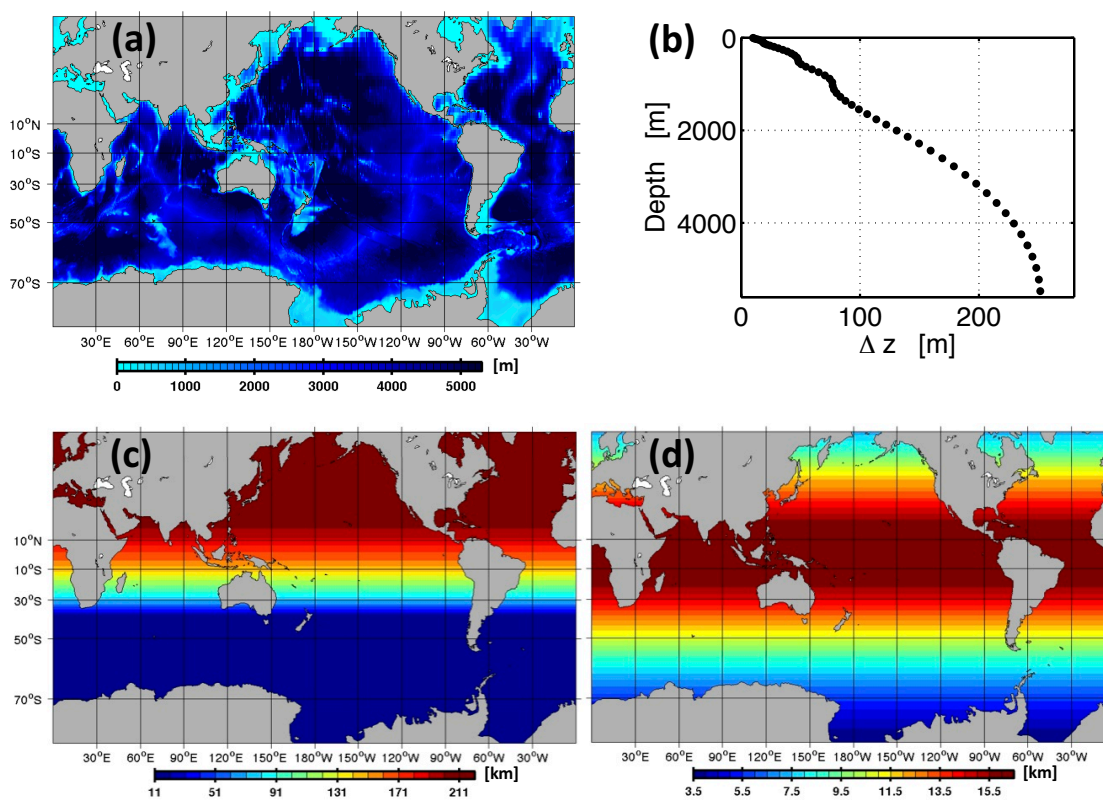
Figure 1. MOMSO model domain and spacial (finite differences) discretization. Panel **(a)** shows the model bathymetry. Panel **(b)**, **(c)** and **(d)** show the vertical, meridional and zonal resolution, respectively. In total, there are $2400 \times 482 \times 55$ grid boxes in zonal, meridional and vertical direction, respectively.
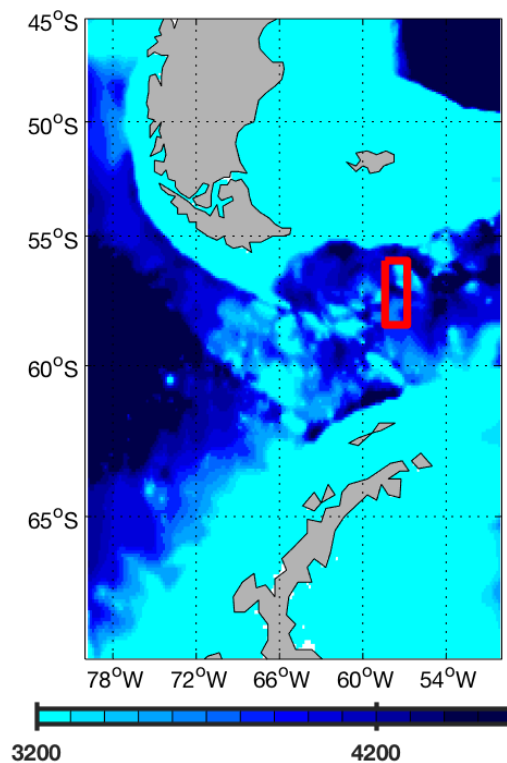
Figure 2. Closeup of MOMSO bathymetry in the Drake Passage. The color denotes depths in meters. The red rectangle denotes the area where, from 3250 m down to the bottom, an additional Laplacian horizontal viscosity of $1000\,m^2/s$ is applied for stability reasons.
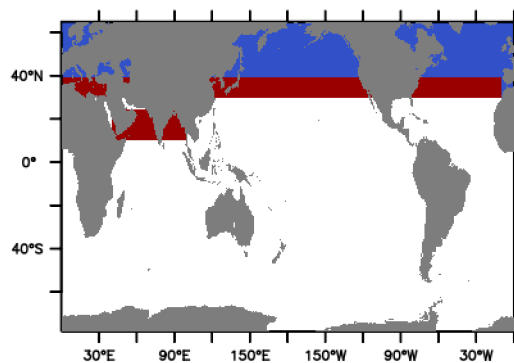
Figure 3. MOMSO domains where temperature and salinity are restored to observed climatological values (Locarnini et al., 2010; Antonov et al., 2009, , respectively) throughout the water column. The red and blue patch denote e-folding restoring timescales of 10 and 5 years, respectively.
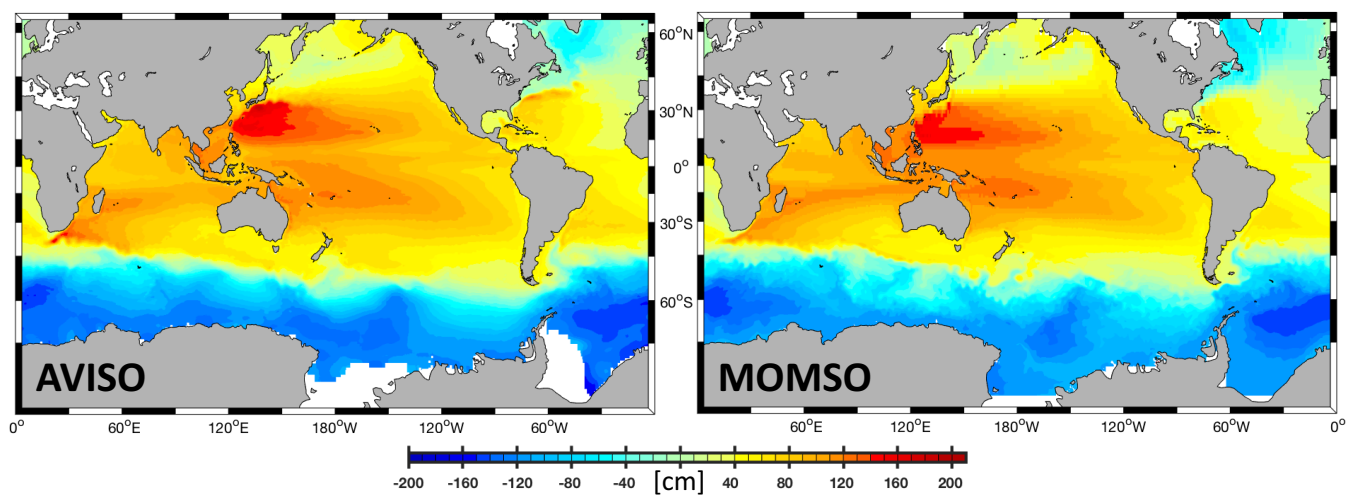
Figure 4. Climatological mean sea surface height in units *cm*. The left panel shows a 1993 to 1998 climatological average observed from space (MADT AVISO data). The right panel shows a 6-year average (nominal years 1993 to 1998) simulated with the reference simulation. White patches in the left and right panel indicate missing data and (spurious) model land mask, respectively.
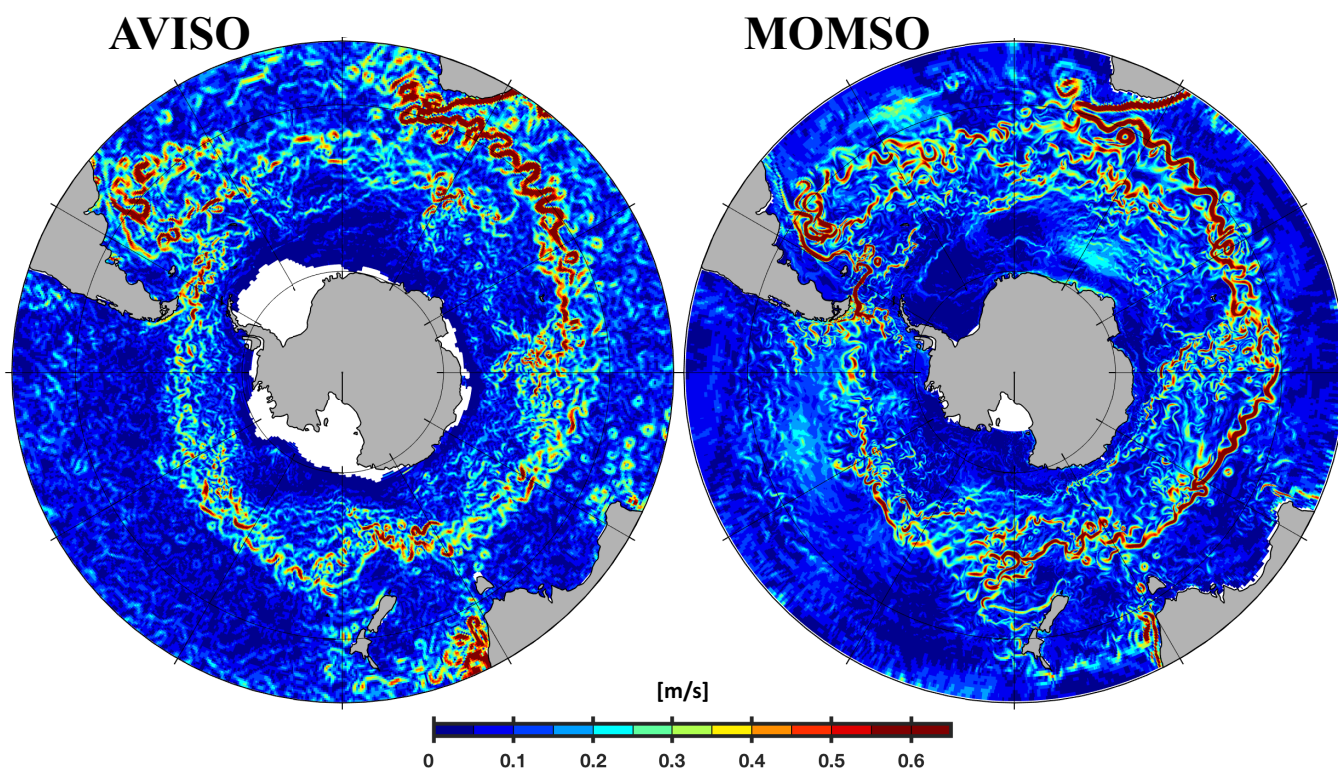
Figure 5. Magnitude of surface velocities. The left and right panel show typical snapshots as observed from space (AVISO, 3rd of May 1995) and as simulated (MOMSO, 3rd of May of nominal year 2020), respectively.
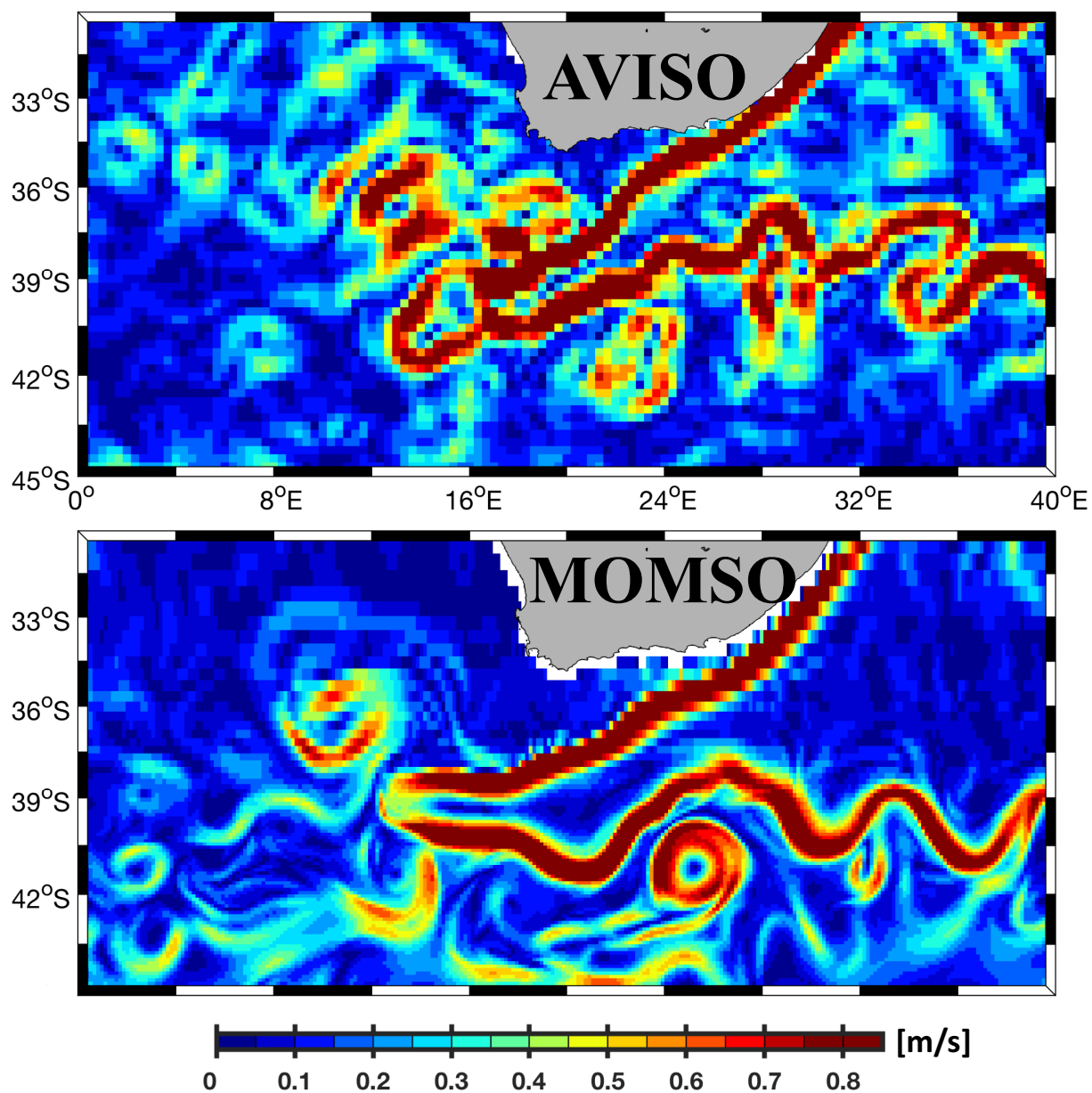
Figure 6. Magnitude of surface velocities. The left and right panel show typical snapshots as observed from space (AVISO, 3rd of May 1995) and as simulated (MOMSO, 3rd of May of nominal year 2020), respectively. This is a closeup from Fig. 5, focussing on those latitudes where the meridional resolution transitions from eddy-permitting in the South to eddy-prohibiting in the North.
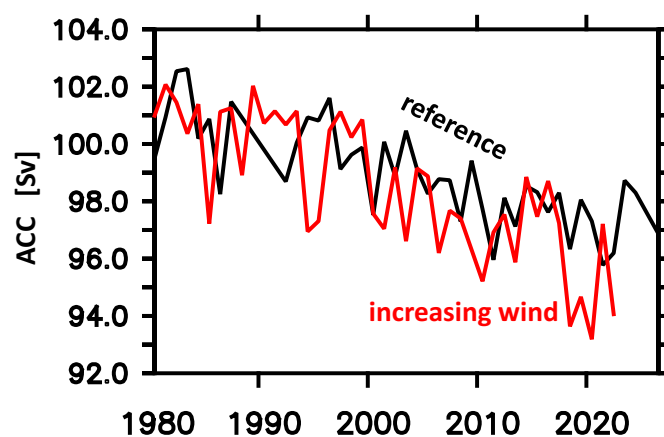
Figure 7. Simulated volume transport of the Antarctic Circumpolar Current through Drake Passage in units $10^6 \, m^3 \, s^{-1}$. The black (red) line refers to the reference (increasing-wind) simulation.
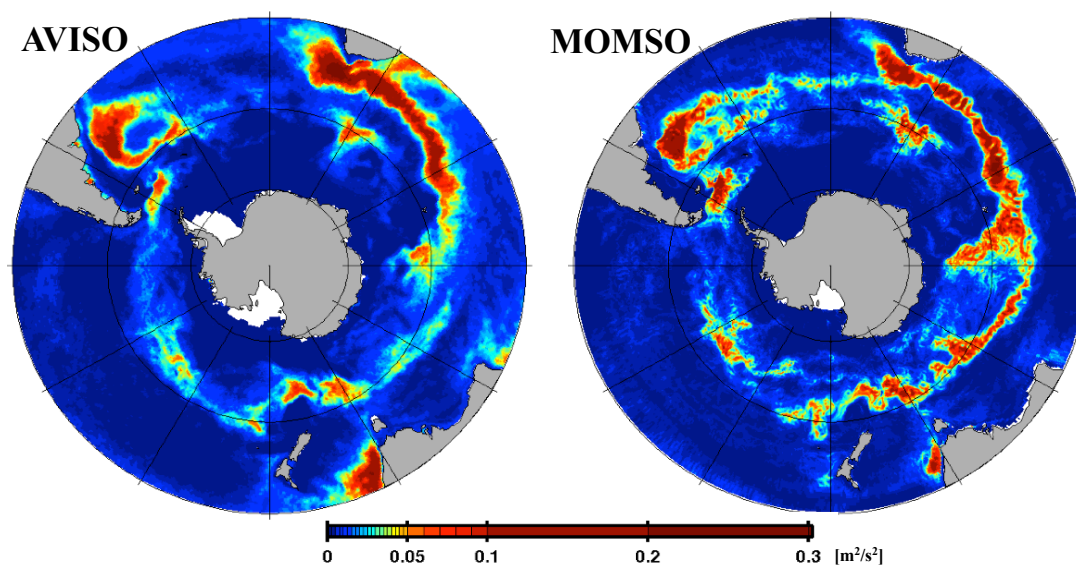
Figure 8. Eddy kinetic energy. The left panel is calculated from 1993-1998 satellite altimetry (MSLA AVISO data) observations. The right panel corresponds to a 6-year average (nominal years 1993 to 1998) calculated from daily-averaged surface velocities from the reference simulation. White patches in the left and right panel indicate missing data and (spurious) model land mask, respectively.
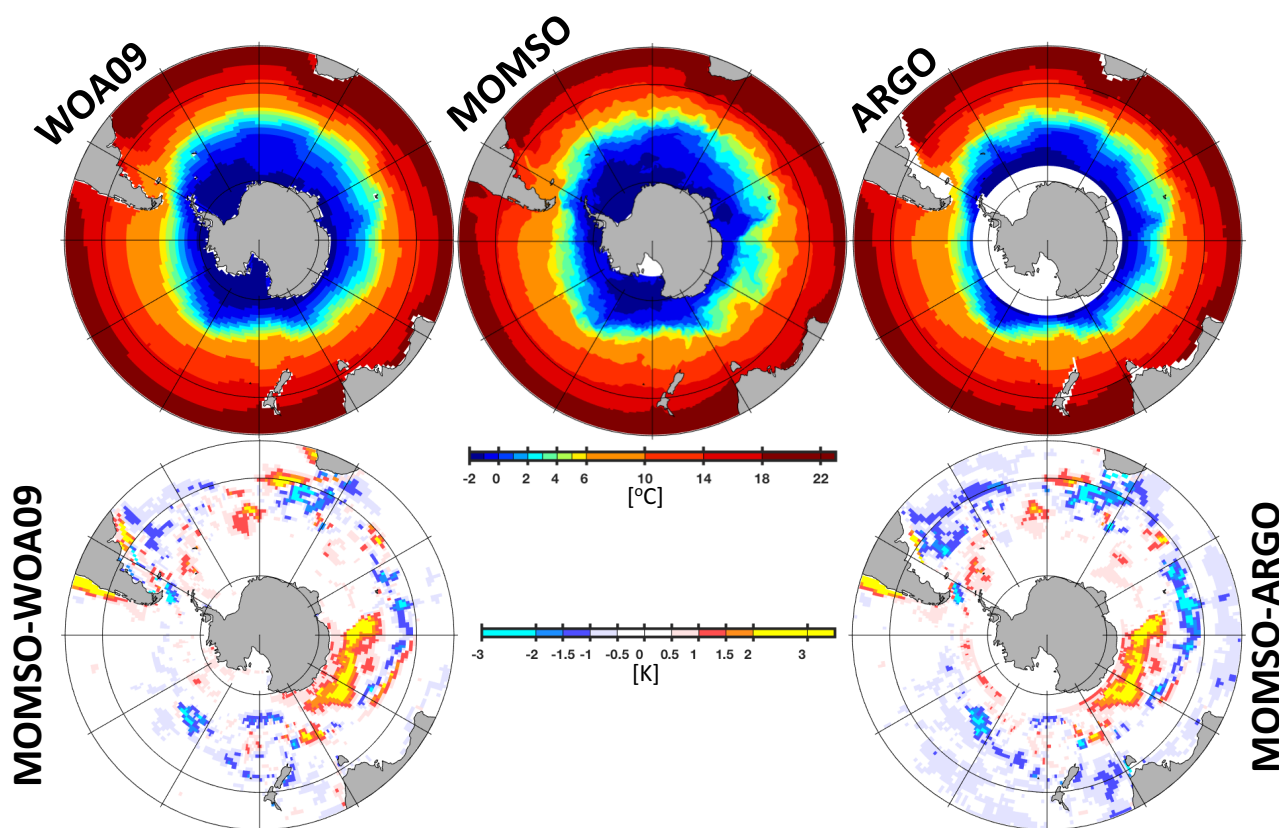
Figure 9. Climatological mean sea surface temperature. WOA09 and ARGO (2004-2017 period) refer to observations compiled by Locarnini et al. (2010), and Roemmich and Gilson (2009), respectively. MOMSO refers to an average over the nominal 1993-1998 period of the reference simulation. The upper (lower) panels show sea surface temperature (differences).
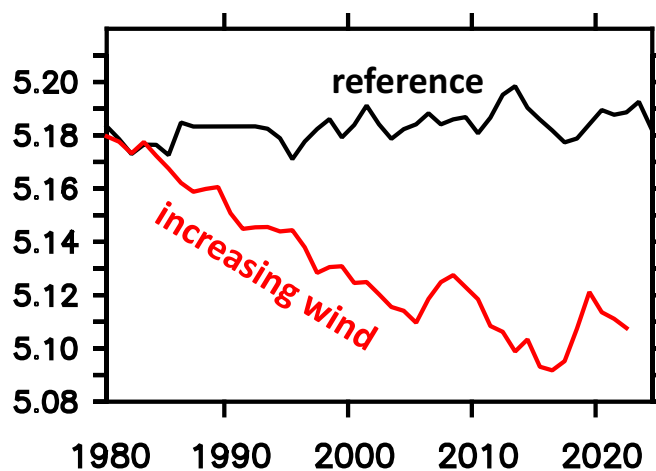
Figure 10. Simulated sea surface temperature averaged over the Southern Ocean (i.e. south of $40°$S). The black (red) line refers to the reference (increasing-wind) simulation.
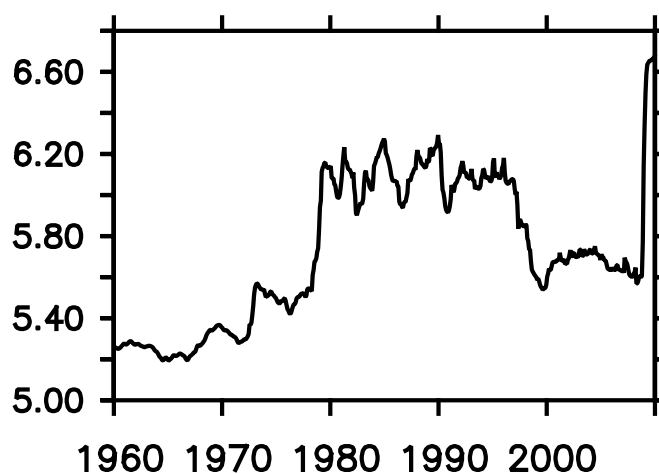
**Figure 11.** Observational estimate of annual mean sea surface temperatures south of $40°$S calculated from HadISST (Rayner et al., 2003).
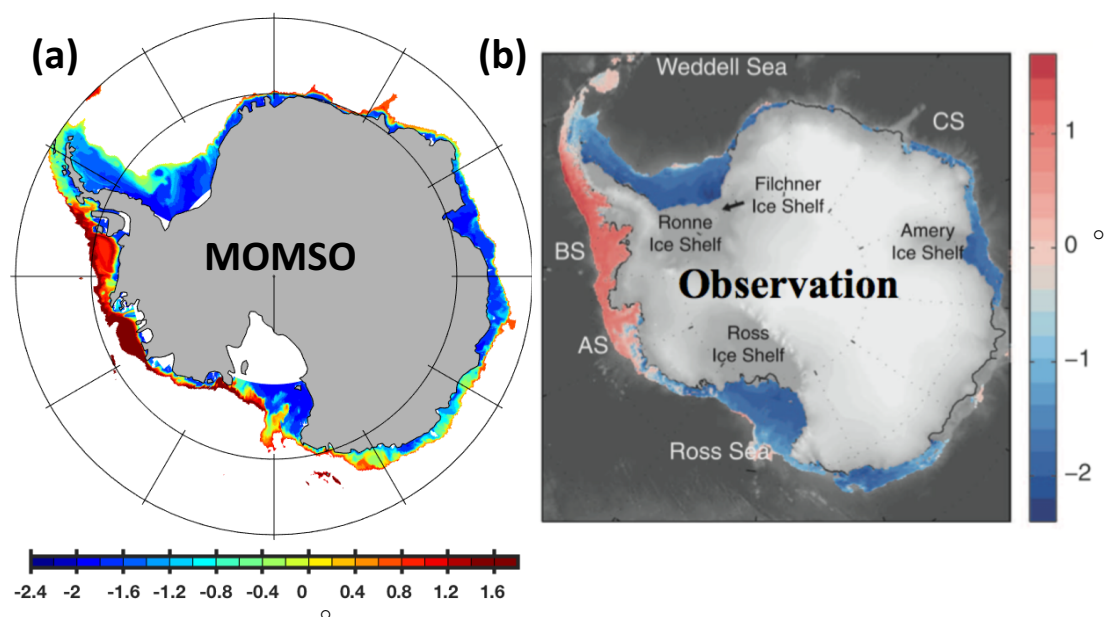
Figure 12. Temperature of Antarctic Continental Shelf Bottom Water (ASBW) at the seabed for depths shallower than 1500 m. Panel **(a)** and **(b)** refer to the simulated 1993 to 1998 climatology and observations compiled by Schmidtko et al. (2014), respectively.
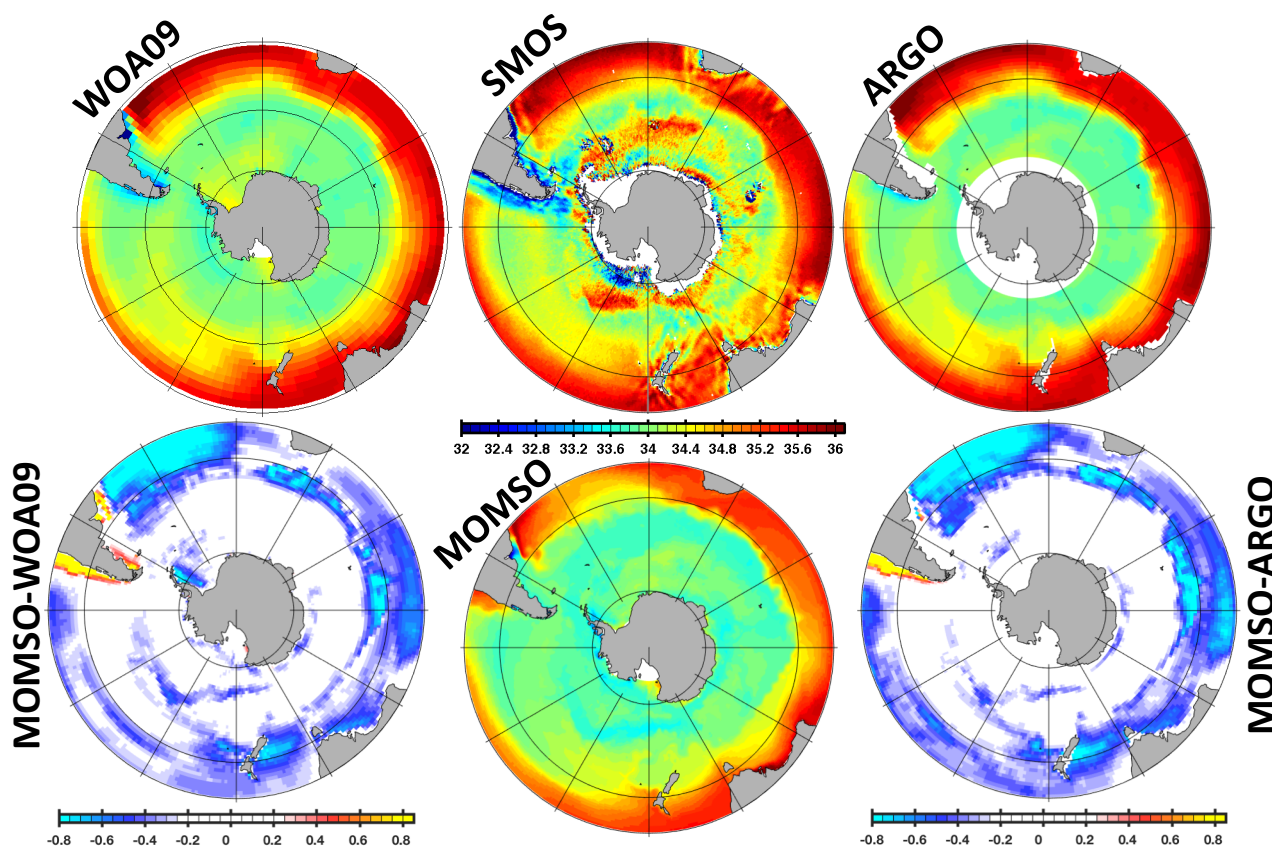
Figure 13. Climatological mean sea surface salinity in units PSU. WOA09, ARGO (2004-2017 period) and SMOS in the upper panels refer to observations compiled by Antonov et al. (2009), Roemmich and Gilson (2009) and Köhler et al. (2015), respectively. MOMSO in the lower panel refers to an average over the nominal 1993-1998 period of the reference simulation. MOMSO-WOA09 and MOMSO-ARGO refer to sea surface salinity differences between the reference simulation and respective observations.
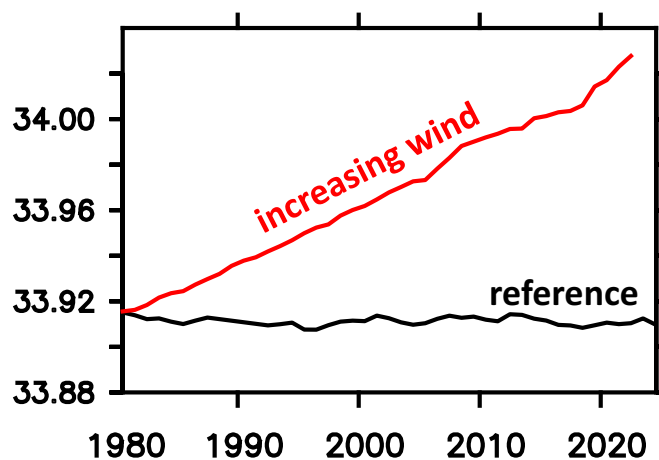
Figure 14. Simulated sea surface salinity averaged over the Southern Ocean (i.e. south of $40°$S) for the nominal years 1980 – 2024. The black (red) line refers to the reference (increasing-wind) simulation.
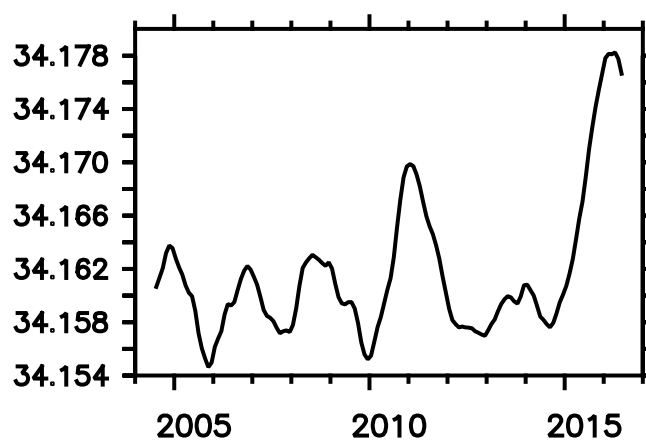
Figure 15. Observed sea surface salinity averaged over the Southern Ocean (i.e. south of $40°$S) based on ARGO data (Roemmich and Gilson, 2009).
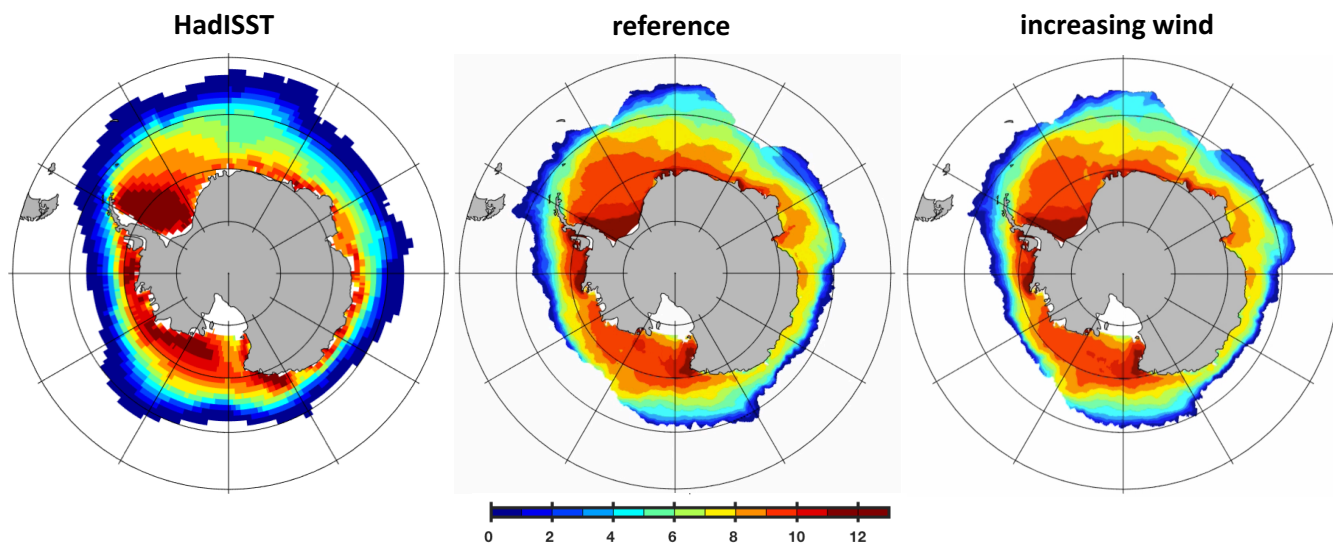
Figure 16. Ice-covered months in a year. The left panel refers to a 1980 to 2000 average based on the HadISST observational estimate (Rayner et al., 2003). The middle and right panel refer to the nominal year 2022 of the reference and increasing-wind simulation, respectively.
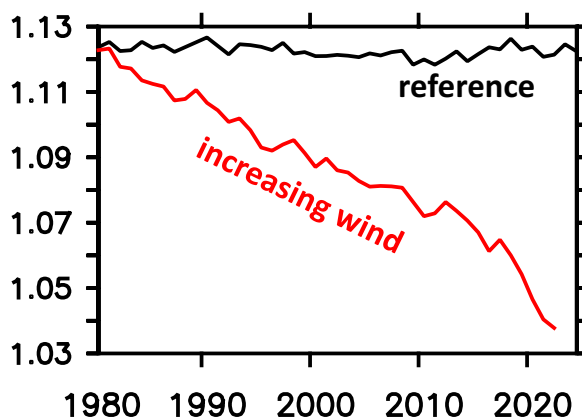
Figure 17. Simulated annual mean sea ice cover south of $40°$S in units $10^7\,km^2$. The black (red) line refers to the reference (increasing-wind) simulation.
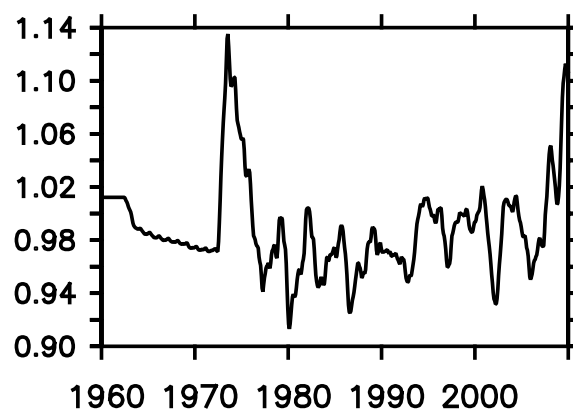
Figure 18. Observational estimate of annual mean sea ice cover south of $40°$S in units $10^7\,km^2$ calculated from HadISST (Rayner et al., 2003).
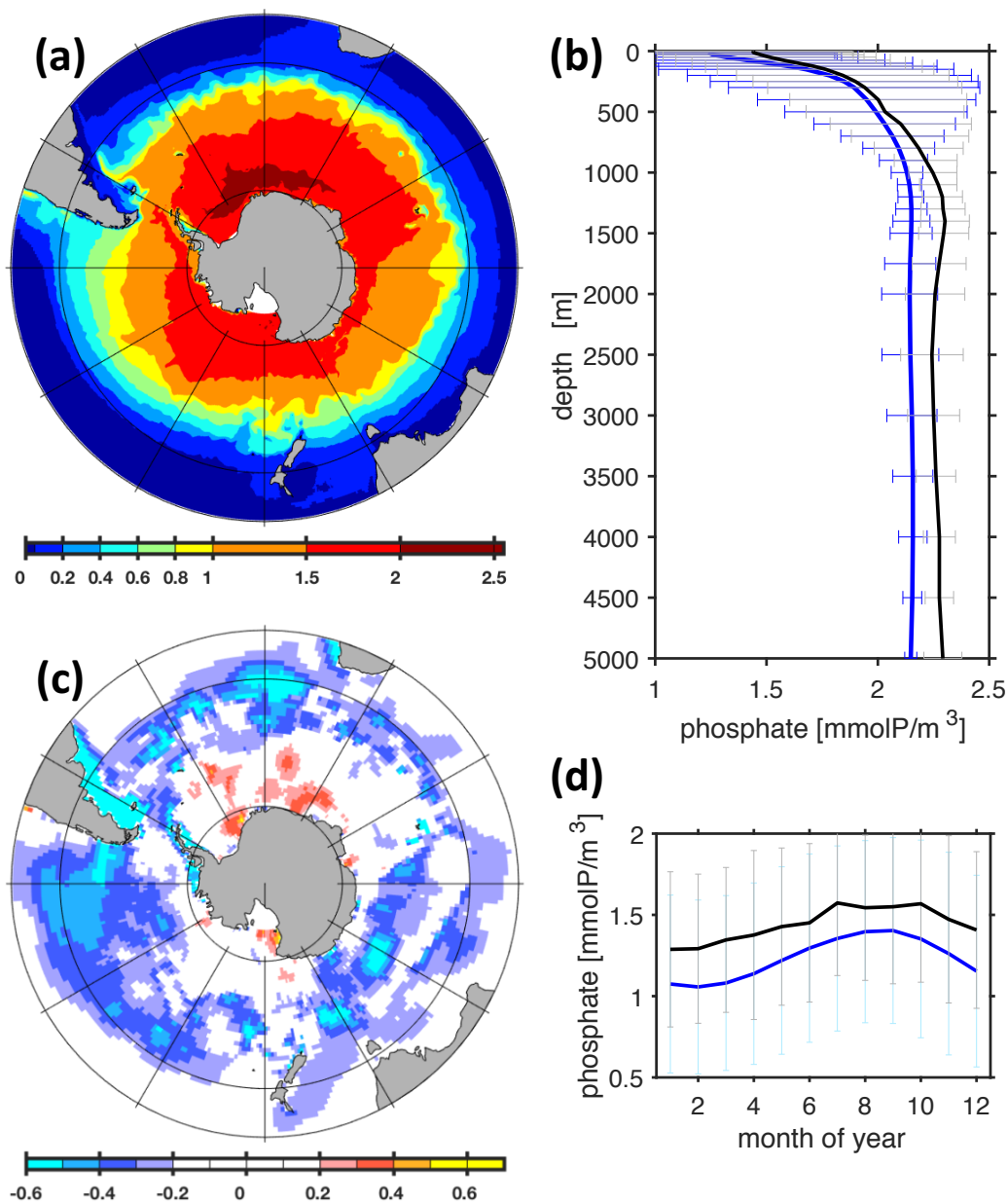
Figure 19. Comparison of simulated and observed phosphate concentrations. Panel **(a)** refers to simulated surface phosphate concentrations (reference simulation, averaged over nominal years 1993 to 1998). The colorbar denotes phosphate concentrations in units $mmol\,P\,m^{-3}$. Panel **(b)** shows simulated (blue line) and observed (black line) phosphate concentrations averaged horizontally in the Southern Ocean (i.e. south of $40°\mathrm{S}$) along with their respective spatial standard deviations (grey and blue horizontal bars). Pannel **(c)** shows the difference between simulated and observed (Garcia et al., 2010) surface concentrations. Panel **(d)** shows the simulated (blue line) and observed (black line) seasonal cycle of dissolved phosphate concentration at the surface calculated as monthly means averaged over the Southern Ocean.
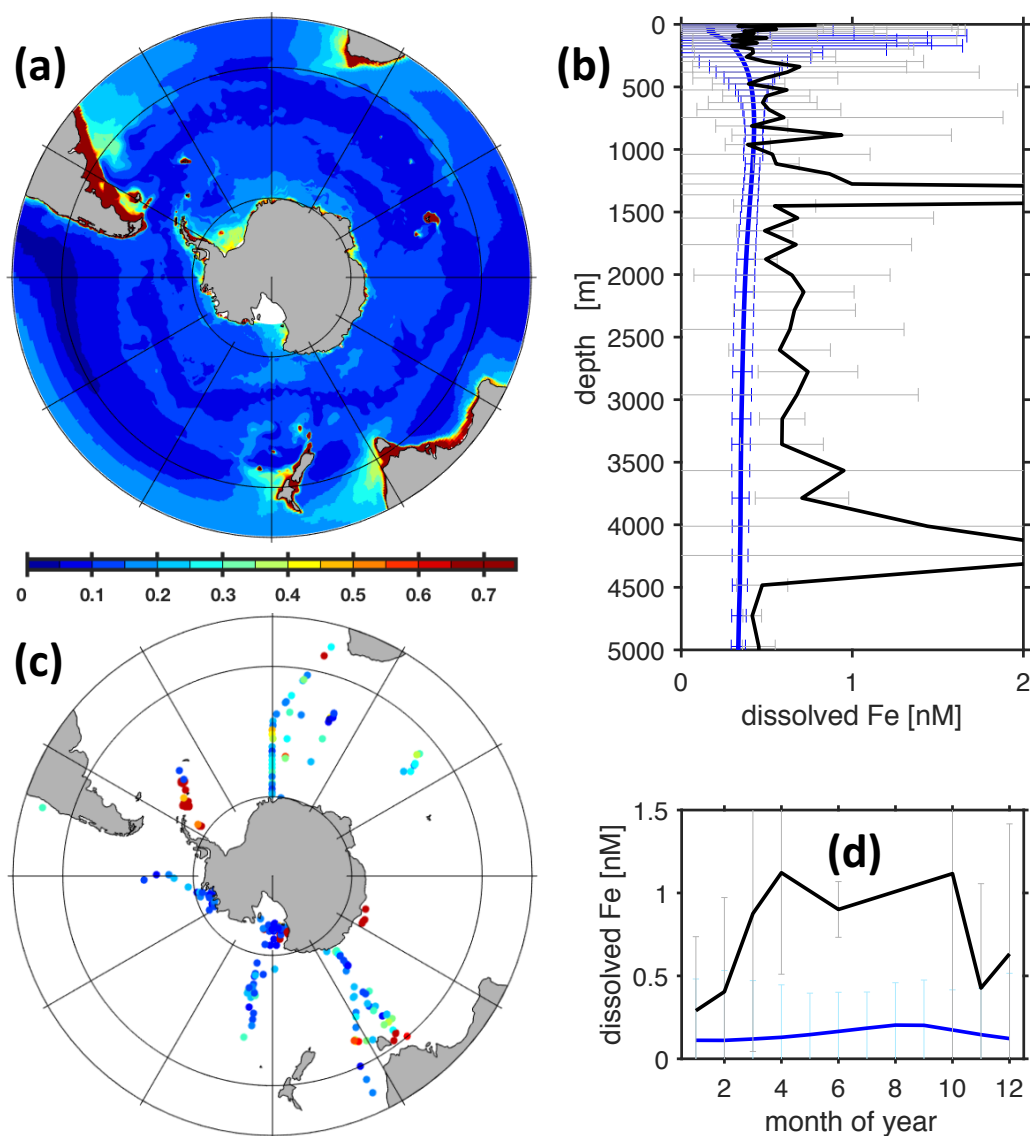
Figure 20. Comparison of simulated with observed dissolved iron concentrations. Panel **(a)** refers to simulated surface iron concentrations (reference simulation, averaged over nominal years 1993 to 1998). The colorbar denotes iron concentrations in units $nM\,Fe$. Panel **(b)** shows simulated (blue line) and observed (black line) concentrations averaged horizontally in the Southern Ocean (i.e. south of $40°\,S$) along with their respective spatial standard deviations (grey and blue horizontal bars). Panel **(c)** refers to observed surface iron concentrations (compiled by Tagliabue et al. (2012) & Mawji, E., et al. (2014)). (The colorbar matches Panel a). Panel **(d)** depicts the simulated (blue line) and observed (black line) seasonal cycle of dissolved iron concentration at the surface calculated as monthly means averaged over the Southern Ocean.
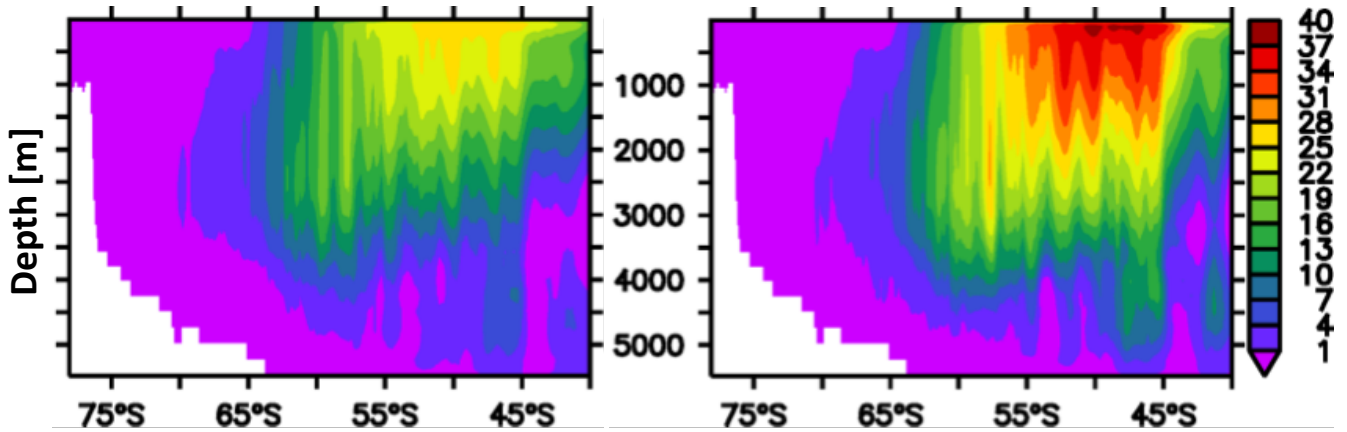
Figure 21. Simulated Southern Ocean meridional overturning circulation in units $10^6\,m^3\,s^{-1}$ averaged over nominal year 2024. The left (right) panel refers to the reference (increasing WIND) simulation.
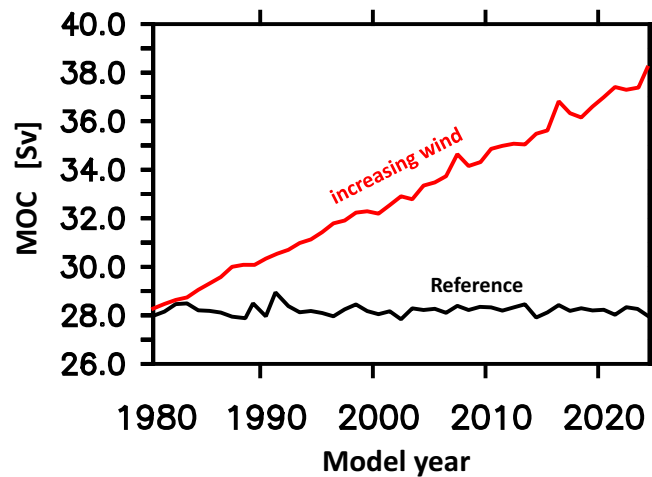

Figure 22. Maximum Southern Ocean meridional overturning circulation south of $40°$S in units $10^6\,m^3\,s^{-1}$. The black (red) line refers to the reference (increasing-wind) simulation.
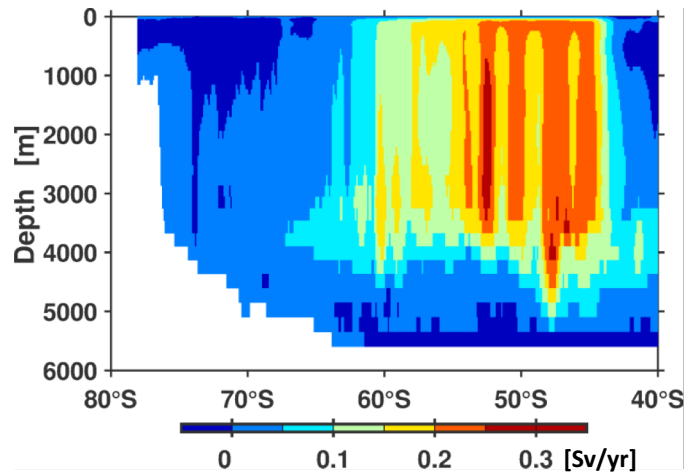
Figure 23. Simulated linear trend of Southern Ocean meridional overturning circulation effected by increasing winds during nominal years 1980 to 2024 in units $10^6\,m^3\,s^{-1}\,yr^{-1}$. Positive values denote increasing overturning.
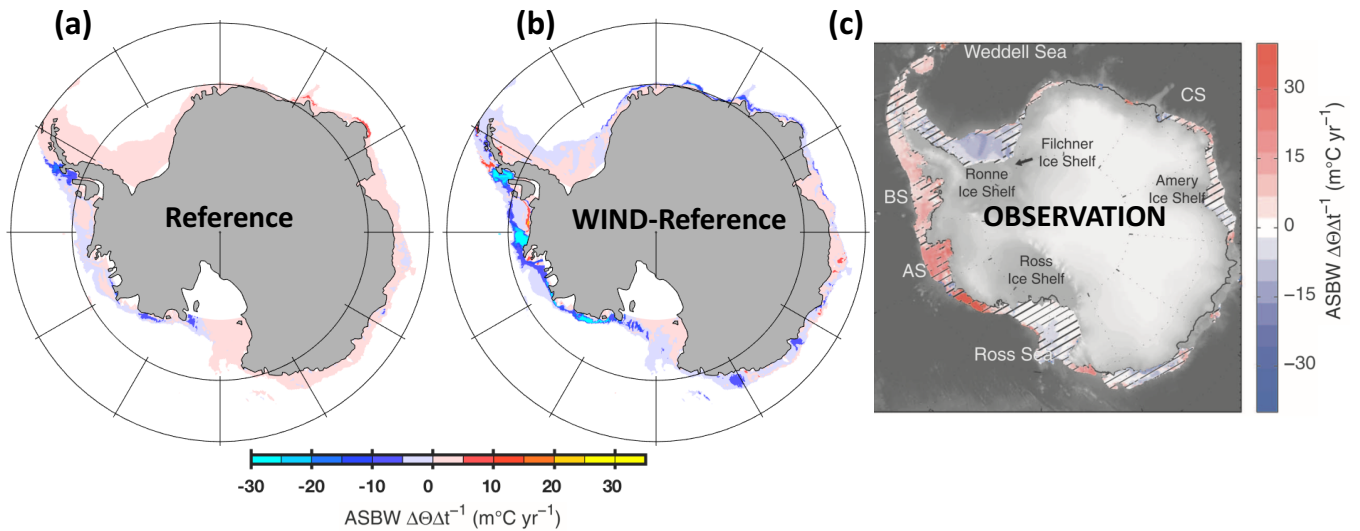

Figure 24. Temporal trend in the temperature of the Antarctic Continental Shelf Bottom Water (ASBW) at the seabed for depths shallower than 1500 m. Panel **(a)** refers to the drift that is still persistent in the reference simulation during nominal years 1980 to 2024. **(b)** refers to the trend in simulation in the simulation with increasing winds corrected by the drift that still persists in the reference. Panel **(c)** refers to an observational estimate compiled by Schmidtko et al. (2014).
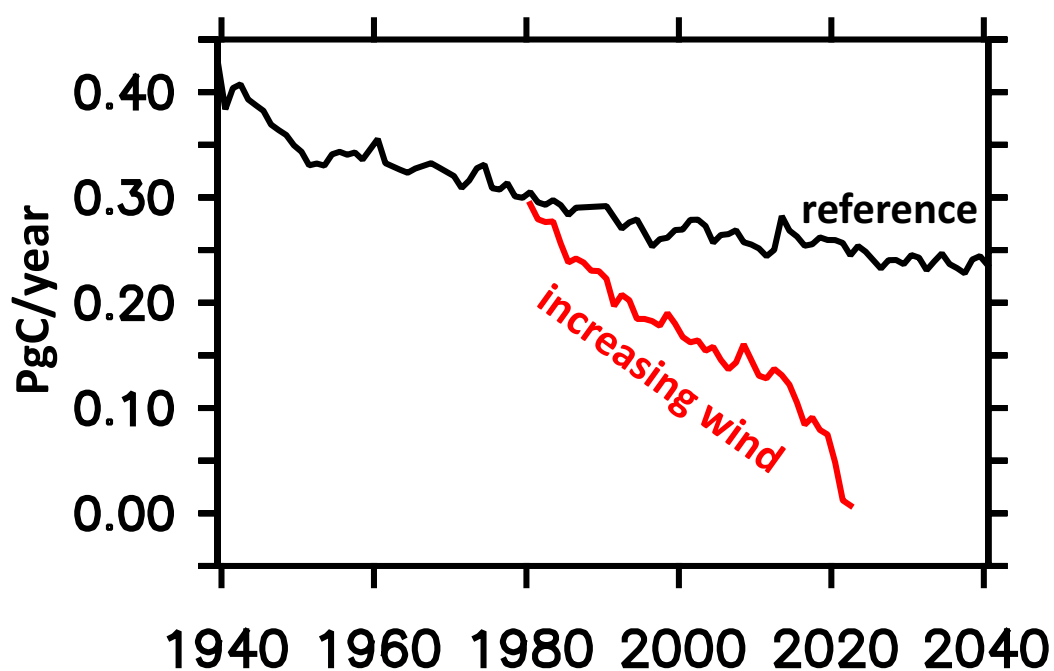
Figure 25. Simulated oceanic uptake of natural carbon south of $40°$S. The black (red) line refers to the reference (increasing-wind) simulation.
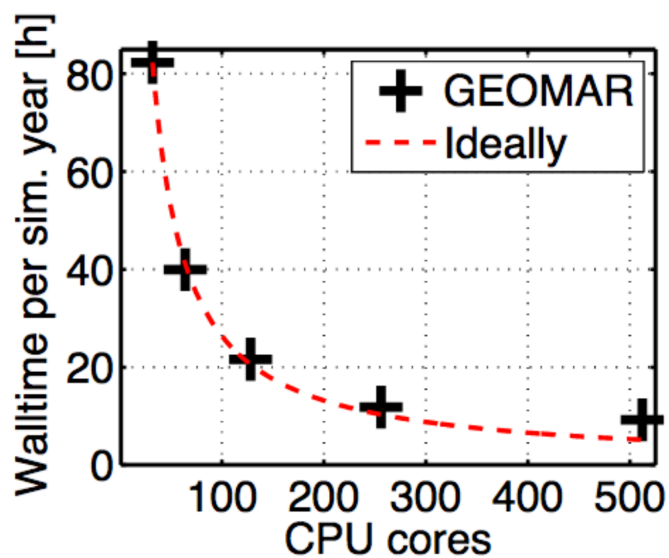
Figure 26. Computational performance as a function of CPU cores put to work simultaneously. On 500 Intel Xeon CPU E5-2670 cores it takes 10 hours to simulate one year.